frontiers | Frontiers in Earth Science

TYPE Original Research
PUBLISHED 14 September 2023
DOI 10.3389/feart.2023.1237495

OPEN ACCESS

EDITED BY
Ali Abedini,
Urmia University, Iran

REVIEWED BY
Akram Alizadeh,
Urmia University, Iran
Rongxi Li,
Chang'an University, China

*CORRESPONDENCE
Yong Li,
liy@cdut.edu.cn

RECEIVED 09 June 2023
ACCEPTED 31 August 2023
PUBLISHED 14 September 2023

CITATION
Zhao L, Li Y, Zou C, Zhao S and Wu C (2023), Paleoenvironmental characteristics and organic matter enrichment mechanisms of the upper Ordovician-lower Silurian organic-rich black shales in the Yangtze foreland basin, South China.
Front. Earth Sci. 11:1237495.
doi: 10.3389/feart.2023.1237495

Paleoenvironmental characteristics and organic matter enrichment mechanisms of the upper Ordovician-lower Silurian organic-rich black shales in the Yangtze foreland basin, South China

Liang Zhao[1], Yong Li[2]*, Chengjie Zou[3], Shaoze Zhao[3] and Chaorong Wu[2]

[1]College of Energy, Chengdu University of Technology, Chengdu, China, [2]College of Geophysics, Chengdu University of Technology, Chengdu, China, [3]College of Earth Sciences, Chengdu University of Technology, Chengdu, China

The Wufeng Formation-Longmaxi Formation (O_3w-S_1l_1) black shales within the Yangtze foreland basin (South China) hold significant potential as unconventional oil and gas resources. However, several challenges, including sluggish sedimentation rates, thin sedimentary layers, and notable homogeneity, hinder a comprehensive grasp of the organic matter enrichment (OME) mechanism within these shales. These challenges impede the exploration of unconventional oil and gas resources. This study aims to identify the O_3w-S_1l_1 black shales in the Weiyuan area through a combined approach of organic and inorganic geochemical analyses. By doing so, it delves into the controlling mechanism behind OME in the black shales of the Yangtze foreland basin. The findings of this research reveal that the O_3w-S_1l_1 black shales primarily consist of sapropelic kerogen and exhibit signs of over-maturation, with TOC content ranging from 0.43% to 8.21%. These shales are classified as organic-rich, mainly composed mixed and siliceous lithofacies. The presence of silica in the shales originates mainly from biogenic sources, and the highest TOC content coincides with a Si_{xs} contribution of around 30% to the total silica content. During the late Katian, a global sea level drop led to an oxic paleoenvironment, transitioning into a euxinic paleoenvironment as sea levels rose in the early Rhuddanian. Notably, TOC content exhibited a significant correlation with paleoceanographic conditions (e.g., V/Cr, Ni/Co) and paleoproductivity levels (e.g., P/Al, Ba_{bio}), while displaying a negative correlation with paleoclimate conditions (e.g., CIA, C-value), terrigenous detrital input intensity (e.g., Si_{xs}, Ti/Al), and sedimentation rate ($(La/Yb)_N$). Specifically, favourable conditions for OME encompass robust reducing seawater conditions, high paleoproductivity, a humid climate, reduced influx of terrigenous debris, and relatively elevated sedimentation rates. Regional tectonic movements (Guangxi movement) and fluctuations in relative sea levels exert influence over the deposition of O_3w-S_1l_1 black shales. This study provides a valuable case study for exploring and developing shale gas resources within the Yangtze foreland basin.

KEYWORDS

paleoenvironment, organic matter enrichment, geochemical characteristics, O_3w and S_1l_1 black shales, the Yangtze foreland basin

1 Introduction

The increasing global energy demand and declining conventional oil and gas resources have emphasized the significance of developing unconventional gas reservoirs, such as shale gas, tight gas, and coalbed methane. The marine organic-rich black shales at the O_3w-S_1l_1 in the Sichuan Basin is considered the most promising layer for shale gas production and the primary target for shale gas commercial development in China (Zou et al., 2019; Yan et al., 2021; Guo et al., 2022). The extensive development of medium and large shale gas fields, including Weiyuan, Changning, and Fuling, has affirmed the immense exploration potential of shale gas reservoirs as "self-generated and self-stored" gas reservoirs (Liang et al., 2009; Nie et al., 2017; Qiu and Zou, 2020a; Ding et al., 2023; Feng et al., 2023).

Numerous studies have been conducted by domestic and foreign scholars on the sedimentology, sequence stratigraphy, paleontology, and geochemistry of the O_3w-S_1l_1 (Zou et al., 2018; Rong and Huang, 2019; Dahl et al., 2021). They believe black shale is an organic-rich sedimentary rock with a close positive correlation between gas and total organic carbon (TOC) content (Liu et al., 2011; Cai et al., 2020). Furthermore, its organic matter enrichment (OME) is closely related to significant global or regional geological and environmental events (Qiu and Zou, 2020b). The O_3w-S_1l_1 were formed during a turbulent geological period (Late Ordovician-Early Silurian transition), experiencing the Hirnantian glaciation (Delabroye and Vecoli, 2010; Melchin et al., 2013; Pohl et al., 2017), biotic extinction (Zou et al., 2018; Dahl et al., 2021; Kozik et al., 2022), ocean anoxia (Melchin et al., 2013), sea level changes (Haq and Schutter, 2008; Lu et al., 2020), and volcanic eruptions (Su et al., 2009; Chen et al., 2014; Xu et al., 2016; Shu, 2021). The complex sedimentary processes result in significant heterogeneity of organic matter (OM) content under different sedimentary environments. As confirmed by considerable research, OME in black shales is regulated by various factors such as paleoredox conditions, paleoproductivity levels, and terrigenous detrital input (Tyson and Pearson, 1991; Feng et al., 2023; Li et al., 2023). Paleoredox conditions are crucial for preserving and accumulating OM; paleoproductivity levels serve as the bedrock for OME; terrigenous detritus input can diminish the abundance of OM (Bornemann et al., 2005).

However, previous studies on OME have mainly concentrated on the relationship between organic-rich shales and paleoenvironments (Li et al., 2023). In contrast, research on regionality paleogeography and paleoenvironments has been limited. The Weiyuan area, influenced by the Zigong uplift, exhibits distinct spatial and temporal variations in OME compared to open water areas such as Changning. This study focuses on the black shales of the O_3w-S_1l_1 in the Weiyuan of the Yangtze foreland basin, investigating the primary factors influencing OME and developing an OME mechanism. Our analysis and research provide a foundation for studying tectonic and paleogeographic changes during the Late Ordovician-Early Silurian in the Yangtze foreland basin, offering scientific support for efficient shale gas development and case studies for identifying new exploration areas.

2 Geological setting

The collision between the Yangtze Block and Cathaysia Block during the Neoproterozoic era led to the formation of the South China Plate. In the Ordovician-Silurian transition period (OST), the South China Plate was situated in a tectonically active region near the ancient equator on the northern edge of the Gondwana continent. During this period, the South China Plate underwent a counterclockwise rotation of approximately 90° from its present position, as depicted in Figure 1A (Zou et al., 2018).

During the OST, the South China Plate mainly experienced intracontinental orogeny deformation, forming a large-scale intracontinental foreland basin system (Shu et al., 2015; Zhang J. et al., 2017; Shu, 2021). The geological structure of the Yangtze foreland basin system mainly comprises forebulge, foreland ramp, foredeep, and orogenic belt (Figure 1B). The Chuanzhong uplift, a flexural uplift associated with the tectonic load of the Cathaysia orogenic belt, is situated to the northwest of the Yangtze foreland basin. To the southeast lies the foreland ramp (Upper Yangtze Basin) and the foredeep (Xiangzhong Basin), which resulted from flexural subsidence. The Cathaysia orogenic belt, extending northeastward like a mountain or island chain, represents the primary source area of the foreland basin (He, 2022). The Yangtze foreland basin is surrounded by the Motianling uplift, Hannan uplift, Chuanzhong uplift, Qianzhong uplift, Zigong uplift, and Yichang uplift, forming a semi-closed marine bay facing northward (Wang et al., 2016; Liang et al., 2017; Wang et al., 2018). Figure 1C demonstrates that the Zigong uplift significantly influences the deposition of organic-rich shales in the Weiyuan area.

The shale sequence of the OST in the Yangtze foreland basin comprises three formations in ascending order: Wufeng Formation (Katian), Guanyinqiao Formation (Hirnantian), and Longmaxi Formation (Rhuddanian). During the post-glacial epoch, the Rhuddanian stage deposited Longmaxi-1 (S_1l_1) under the influence of rising sea levels. S_1l_1 composes of black shales and grey muddy siltstone and can be divided into subunits $S_1l_1^1$ and $S_1l_1^2$. The thickest gas-bearing layer is $S_1l_1^1$, which has a thickness of 54.3 m. Logging data indicates apparent stratification in the O_3w-S_1l_1. The comparison of natural gamma-ray logging (GR) and gamma-ray without uranium (KTH) shows higher uranium (U) content in $S_1l_1^1$. Additionally, there is a significant positive correlation between mud and U content in the sedimentary rocks, indicating higher mud content in this section. Comparison of the compensated neutron logging (CNL) reflects a higher porosity in this section, as shown in Figure 1D. Considering the TOC content, $S_1l_1^1$ presents a promising target for the exploration and development of shale gas in the Weiyuan area.

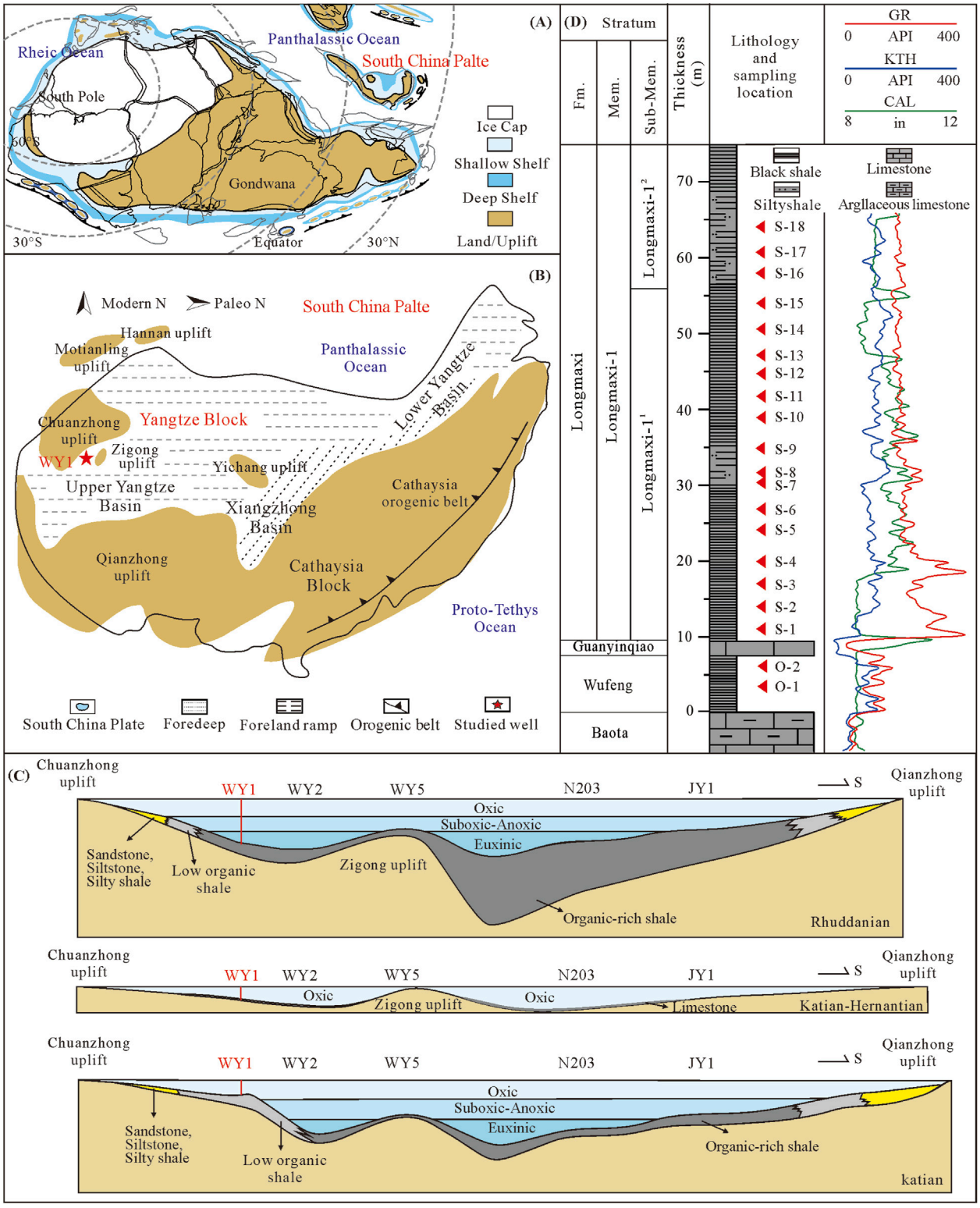

FIGURE 1
(A) The Paleogeographic of the South China plate in the Late Ordovician (445 Ma) (Zou et al., 2018); **(B)** The Yangtze foreland basin system and well location (Guo, 2014); **(C)** Sedimentary evolution model of organic-rich shales in the Weiyuan area (Liang et al., 2017); **(D)** The schematic stratigraphic histogram and sampling location of WY1.

3 Sampling and methods

3.1 Sampling

The Weiyuan area is a well-preserved specimen of the O-S foreland ramp in the Yangtze foreland basin, retaining stratigraphic and tectonic characteristics. The stratum sequence shows almost no deformation or displacement, remaining *in situ* with complete structural integrity. Therefore, the output state of shale basically reflects the ancient tectonic state at that time and the current preservation state. The high-quality coring from Well WY1 provides essential information on the lithofacies types and sedimentary environmental evolution of the O_3w-S_1l_1 organic-rich black shales in the study area. To prevent weathering from influencing the samples, this study selected twenty samples of the O_3w-S_1l_1 formation from the Well WY1 core at an average sampling interval of approximately 3–4 m, including two samples of O_3w and eighteen samples of S_1l_1. For detailed information on the sample numbers, stratigraphic positions, and lithological characteristics, as shown in Figure 1D. All test analysis is completed in the Analysis Experiment Center of Exploration and Development Research Institute of Petrochina Southwest Oil and Gasfield Company. Before submission, samples are ground to 200 mesh for mineralogical and geochemical analysis.

3.2 Analytical methods

Selected core samples were meticulously prepared for analysis through rough crushing, rinsing with deionised water, drying, and pulverisation to obtain a fine powder. The powder was then passed through a 200-mesh sieve and stored in polypropylene bags for subsequent testing.

To determine the mineralogical compositions, the samples were ground to a powder with a grain size of less than 40 μm and analysed using X-ray diffraction (XRD, X'Pert Pro MPD, Nalytical, Netherlands). The analysis operated Cu Kα radiation at 40 kV and 40 mA and a scan over a range of 5°–45° (2θ). The experimental procedures were by SY/T 5163-2010. The WPF module of JADE 9.0 software was used to determine semi-quantitative phase abundances through Rietveld refinement by identifying mineral species using characteristic mineral diffraction peaks.

Mix polyvinyl alcohol and distilled water in a 1:9 to 1:11 ratio to prepare a polyvinyl alcohol solution through heating and slow stirring. Mix the shale sample with the polyvinyl alcohol solution to make a thin film, and use a polarising microscope (AxioScope A1 type) to identify and measure macerals and component content.

After drying the samples, send the shale sample to a rock pyrolysis analyser for thermal analysis of the rock. The experimental procedures were following GB/T 18602-2012.

To remove inorganic carbon and carbonate minerals, samples were soaked in a hydrochloric acid and water mixture at 1:9. The total organic carbon content was calculated by testing the samples using a Leco CS-230 carbon sulfur analyser. The experimental procedures followed by GB/T 19145-2003.

Put the sample into the muffle furnace, burn it at 1,000°C, and weigh it again after cooling. The difference in weight before and after heating the residues is the LOI (Loss on Ignition). Major element analysis was performed by X-ray fluorescence spectrometry (XRF, Malvern Panalytical PAxios-mAx, Netherlands). After the samples were digested with a mixture of NaOH, and HNO_3, trace elements were measured using an inductively coupled plasma mass spectrometer (ICP-MS, PerkinElmer NexION 350X, United States). The experimental procedures were following GB/T 14506-2010. Quality control was performed using blanks, replicates, and reference materials. For all samples, the analytical results of the reference material were within±10% of the certified value, and the relative standard deviation (RSD) value of the replicates was within 5%.

3.3 Data presentation

(1) The Enrichment Factor (X_{EF}) is a common metric for expressing the degree of enrichment of major and trace elements in shale. Standardizing and calibrating trace elements using Al is essential to eliminate the influence of detrital material derived from the land (Wedepohl, 1971; Tribovillard et al., 2006). The calculation formula of the X_{EF} is as follows:

$$X_{EF} = (X/Al)_{sample} / (X/Al)_{average\ shale} \quad (1)$$

In the formula, X_{EF} stands for the enrichment factor of an element with no units. $(X/Al)_{average\ shale}$ is the ratio of the average element content to Al in shale. An X_{EF} value greater than 1 indicates relative enrichment of the element in shale, while an X_{EF} value less than 1 suggests relative deficiency in comparison to the average shale.

(2) Excess silicon or biogenic silicon (Si_{xs}, Si_{bio}) refers to the residuals obtained by subtracting the estimated silica content of terrigenous detrital input from the total siliceous content. It is mainly of biogenic origin and serves as a standard proxy for paleoproductivity in sediments (Tribovillard et al., 2006; Ross and Bustin, 2009). The calculation formula of the Si_{xs} is as follows:

$$Si_{xs} = Si_{sample} - \left[Al_{sample} \times (Si/Al)_{background}\right] \quad (2)$$

In the formula, Si_{xs} represents the excess silicon content in the sample, Si_{sample} and Al_{sample} refer to the SiO_2 and Al_2O_3, respectively, and $(Si/Al)_{background}$ is 3.11 (Wedepohl, 1971; Adachi et al., 1986).

(3) Barium (Ba) is a widely used paleoproductivity indicator with multiple sources, including biological sources (Ba_{bio}) and input of terrigenous debris. Ba_{bio} is the only parameter that reflects the magnitude of paleoproductivity (Wedepohl, 1971; Dehairs et al., 1987; Paytan et al., 1996; Tribovillard et al., 2006). Modern ocean research suggests that high primary productivity in the sedimentary environment is represented by a Ba_{bio} content ranging between 1000 and

5000 μg/g (Pi et al., 2013; Schoepfer et al., 2015). The calculation formula of the Ba_{bio} is as follows:

$$Ba_{bio} = Ba_{sample} - \left[Al_{sample} \times (Ba/Al)_{background}\right] \quad (3)$$

In the formula, Ba_{sample} and Al_{sample} refer to the Ba and Al_2O_3 contents measured in the samples. The $(Ba/Al)_{background}$ is the ratio of the two elements in the post-Archean Australian shale (PAAS), and the $(Ba/Al)_{background}$ is 0.0077 (Taylor and McLennan, 1985).

(4) Cerium (Ce) has low solubility in seawater but a high concentration in terrigenous sediments. Therefore, sedimentary material of this type frequently notable Ce anomalies (δCe) influenced by terrigenous detrital input. This anomaly can reflect the degree of seawater submergence in the sediment and the intensity of terrigenous detrital input, providing essential indicators of sea level change. A δCe value greater than 1 indicates a positive anomaly signifying euxinic conditions in the water. Conversely, a δCe value less than 1 indicates oxic conditions in the water and is considered a negative anomaly (Elderfield and Greaves, 1982; Baar et al., 1985; Murray et al., 1991; Wilde et al., 1996). The calculation formula of the δCe is as follows:

$$\delta Ce = Ce_N / (La_N \times Pr_N)^{1/2} \quad (4)$$

In the formula, n is the average shale normalized value.

(5) The Chemical Index of Alteration (CIA) is widely used to determine the intensity of paleochemical weathering in the provenance areas and the characteristics of paleoclimate (Nesbitt and Young, 1984). A CIA value within the range of 85–100 indicates intense chemical weathering, suggesting a hot and humid paleoclimate. A value between 65–85 signifies moderate chemical weathering, representing a warm and humid paleoclimate. CIA values between 50-65 points to initial chemical weathering in the provenance area, reflecting cold and dry paleoclimate. The calculation formula of the CIA is as follows:

$$CIA = \left[n(Al_2O_3)/(n(Al_2O_3) + n(K_2O) + n(Na_2O) + n(CaO^*))\right] \times 100 \quad (5)$$

In addition, CaO in non-silicate minerals needs to be removed when calculating the weathering index. CaO in apatite is removed by P_2O_5, and then CaO* is calculated (McLennan et al., 1993; Nesbitt et al., 1996). The calculation formula of the CaO* is as follows:

$$n(CaO_{residue}) = n(CaO) - n(P_2O_5) \times 10/3 \quad (6)$$

In this formula, if $n(CaO_{remaining}) < n(Na_2O)$, then $(CaO^*) = n(CaO_{remaining})$, whereas if $(CaO_{remaining}) > n(Na_2O)$, then $(CaO^*) = n(Na_2O)$.

(6) The C-value is a critical indicator for assessing the paleoclimate conditions of sedimentary rocks (Getaneh, 2002; Zhao et al., 2007; Cao et al., 2012). Generally, when C-value is more greater than 0.8, it indicates a humid climate; when C-value is between 0.6 and 0.8, it means a semi-humid environment; when C-value is between 0.4 and 0.6, it shows a semi-arid/semi-humid climate; when C-value is between 0.2 and 0.4, it indicates a semi-arid environment, and when C-value is less than 0.2, it means an arid climate. The calculation formula of the C-value is as follows:

$$C - value = \sum(Fe + Mn + Cr + Ni + V + Co)/ \times \sum(Ca + Mg + Sr + Ba + Na) \quad (7)$$

(7) The mineral composition significantly influences fracturing behaviour during development. The brittleness index (Br, %) directly measures the rock's brittleness characteristics (Jarvie et al., 2007; Zhang et al., 2019). It is conventionally considered that a shale exhibits favourable fracturing properties when its brittleness index reaches 40% (Zhang et al., 2018). The calculation formula of the Br is as follows:

$$Br = \frac{\omega_{qtz} + \omega_f + \omega_{cal} + \omega_{py}}{\omega_{qtz} + \omega_f + \omega_c + \omega_{py} + \omega_{cl}} \times 100\% \quad (8)$$

In the formula, qtz, f, c, py and cl are the mass fraction (%) of quartz, feldspar, carbonate minerals, pyrite and clay, respectively.

4 Results

4.1 Geochemistry characteristics

SiO_2 and Al_2O_3 constitute the predominant elements within O_3w-S_1l_1 black shales. The SiO_2 content in the O_3w ranges from 52.11% to 53.75% (avg. 52.93%), while the Al_2O_3 content falls between 12.19% and 21.11% (avg. 16.65%). The SiO_2 content in the S_1l_1 ranges from 42.59% to 77.53% (avg. 57.33%), and the Al_2O_3 content ranges from 9.31% to 18.34% (avg. 14.30%). In O_3w-S_1l_1 black shales, there is clear vertical differentiation in the content of the main elements. As the depth is Shallow, the content of SiO_2 and Na_2O gradually increases while the range of MgO, TiO_2, and MnO decreases. Al_2O_3, Fe_2O_3, and K_2O exhibit a trend of first decreasing and then growing with depth, while CaO and P_2O_5 show a trend of first increasing and then declining (Table 1). Redox-sensitive elements (RSEs), including V, Cr, Th, U, and Mo, are commonly used to reconstruct ancient marine environments (Tribovillard et al., 2006). Most trace elements in O_3w-S_1l_1 black shales are enriched compared to the PAAS, except for Sr and Zr, which are depleted (Table 2 and Table 4). V, Mo, U, and other elements enrich significantly (EF>5).

Rare earth elements (REE) divergence is influenced by variations in the depositional seawater conditions and sedimentation rates (Elderfield and Greaves, 1982; Shields and Stille, 2001; Rimmer et al., 2004; Li et al., 2008). Table 3 and Table 4 list the rare earth element concentrations in the O_3w- S_1l_1 black shales in the study area. The O_3w and S_1l_1 shales exhibit ΣREE values ranging from 189.93 μg/g to 266.94 μg/g (avg. 228.44 μg/g) and 135.68 μg/g to 271.92 μg/g (avg. 173.77 μg/g), all of which surpass the PAAS reference value. For the O_3w shales, the light rare earth elements (LREE), heavy rare earth elements (HREE), and LREE/HREE ratio values range from 172.36 μg/g to 241.88 μg/g (avg. 207.12 μg/g), 17.57 μg/g to 25.06 μg/g (avg. 21.32 μg/g), and 9.81 to 9.60 (avg. 9.71), respectively. Correspondingly, the S_1l_1 shales display these values

TABLE 1 Content of major elements (wt%) in the O_3w-S_1l_1 black shales.

Sample	SiO_2	Al_2O_3	Fe_2O_3	MgO	CaO	Na_2O	K_2O	P_2O_5	TiO_2	MnO
S-18	60.73	17.79	6.89	2.75	0.88	0.89	4.25	0.11	0.67	0.06
S-17	65.78	14.08	5.24	2.13	3.98	0.69	3.41	0.10	0.49	0.09
S-16	58.41	14.68	5.16	2.24	6.50	0.81	3.59	0.13	0.52	0.12
S-15	60.36	18.11	6.52	2.84	1.20	0.81	4.43	0.11	0.59	0.06
S-14	58.98	18.34	6.59	2.94	1.57	0.82	4.46	0.11	0.60	0.06
S-13	61.01	18.10	6.54	2.83	0.97	0.80	4.47	0.12	0.57	0.05
S-12	63.59	15.55	4.83	2.51	3.25	0.72	3.92	0.13	0.56	0.05
S-11	58.01	15.14	5.23	2.64	6.44	0.80	3.69	0.11	0.54	0.09
S-10	69.49	13.77	5.01	2.20	2.03	0.70	3.40	0.10	0.51	0.05
S-9	42.59	14.45	3.75	4.70	13.95	0.69	3.51	0.13	0.62	0.15
S-8	44.34	14.01	3.63	3.03	14.64	0.78	3.31	0.14	0.64	0.10
S-7	49.66	14.31	4.17	3.18	11.63	0.68	3.49	0.21	0.59	0.10
S-6	42.66	11.70	4.37	4.64	15.16	0.86	2.58	0.21	0.52	0.16
S-5	44.13	10.91	3.04	3.53	16.94	0.63	2.71	0.13	0.51	0.15
S-4	55.11	15.51	4.04	2.80	6.72	1.42	3.58	0.11	0.66	0.05
S-3	61.83	11.95	3.45	2.65	7.54	1.05	2.73	0.12	0.60	0.08
S-2	77.53	9.31	2.44	1.65	4.01	0.72	2.36	0.10	0.49	0.04
S-1	61.40	9.71	2.52	2.63	8.25	0.54	2.63	0.37	0.52	0.15
Mean	57.53	14.30	4.63	2.88	6.98	0.80	3.47	0.14	0.57	0.09
O-2	52.11	12.19	3.24	3.12	12.03	0.47	3.69	0.06	0.52	0.25
O-1	53.75	21.11	7.22	2.94	0.91	0.67	5.71	0.10	1.01	0.04
Mean	52.93	16.65	5.23	3.03	6.47	0.57	4.70	0.08	0.77	0.15

at 120.69 μg/g to 245.10 μg/g (avg. 155.59 μg/g), 13.50 μg/g to 28.11 μg/g (avg. 18.18 μg/g), and 4.97 to 10.51 (avg. 8.74). Negative anomalies in Eu and Ce abundance are observed compared with the chondrite. For the O_3w shales, δEu and δCe values fall within the range of 0.56 to 0.56 (avg. 0.56) and 1.17 to 1.23 (avg. 1.20), respectively. As for the S_1l_1 shales, these values vary from 0.56 to 0.89 (avg. 0.64) and 0.78 to 0.93 (avg. 0.88) (Table 4).

The TOC content of O_3w and S_1l_1 black shales ranges from 0.43% to 0.99% (avg. 0.71%) and 0.75%–8.21% (avg. 2.17%), respectively. The hydrocarbon potential (S_1+S_2) ranges from 0.03 mg/g to 0.05 mg/g (avg. 0.04 mg/g) and 0.04 mg/g to 0.14 mg/g (avg. 0.09 mg/g), respectively. The organic macerals in O_3w-S_1l_1 black shales are predominantly sapropelic, with a TI index ranging from 84.70 to 93.20 (avg. 88.95), 86.40 to 96.60 (avg. 91.50), respectively. This indicates that the shale has sapropelic kerogen (Type I), primarily derived from low-level aquatic organisms like graptolites, with the potential for crude oil generation. Vitrinite reflectance (Ro) is a suitable parameter for assessing the maturity of sedimentary hydrocarbon source rocks. In cases where vitrinite is scarce, the bitumen reflectance (Rb) can serve as a substitute parameter. The Ro values of the WY1 well, all exceeding 2.00% (Table 5), were calculated using a formula based on the empirical knowledge of different researchers (Jacob, 1985; 1989). The Ro values and the T_{max} (avg. 535.50°C) indicate that the O_3w-S_1l_1 black shales have reached the gas dryness stage and are dominated by over-maturity (Table 5).

4.2 Mineral compositions and lithofacies types

The mineral composition of the O_3w-S_1l_1 black shales in the study area is primarily composed of quartz, clay mineral, feldspar, calcite, and pyrite, in descending order. The quartz content in the black shales decreases gradually with increasing depth, accompanied by a corresponding increase in clay mineral content. The changes in other mineral contents are insignificant, as shown in Figure 2A and Table 6. The brittleness index (Br, %) of the O_3w and S_1l_1 black shales range from 63.64% to 65.67% (64.66%) and 32.30%–86.29% (avg. 62.76%), respectively. These values suggest a susceptibility of the mineral composition in these shales to undergo hydraulic fracturing transformations during subsequent stages (Huo et al., 2018).

Choose three groups of mineral components for shale lithofacies classification: siliceous minerals (QFM, quartz+feldspar), clay minerals, and carbonate minerals (calcite+dolomite). The

TABLE 2 Content of trace elements (ug/g) in the O_3w-S_1l_1 black shales.

Sample	V	Cr	Co	Ni	Rb	Sr	Zr	Mo	Ba	U	Th
S-18	169.17	121.12	24.92	67.94	180.08	233.88	136.82	3.56	3631.54	4.61	15.16
S-17	180.93	78.66	15.73	57.10	137.60	120.45	95.69	5.78	775.86	5.50	12.92
S-16	160.04	85.32	15.21	46.43	142.32	168.98	184.63	5.01	718.10	6.91	14.73
S-15	161.54	97.44	18.46	51.27	187.47	111.47	112.93	2.10	687.20	4.15	16.69
S-14	187.21	111.27	19.26	61.61	188.53	142.93	123.80	2.62	3152.78	4.00	16.84
S-13	165.56	82.98	17.90	52.71	182.46	97.36	118.85	2.00	688.61	4.06	15.31
S-12	186.25	101.93	14.92	65.10	156.36	120.36	84.53	1.78	604.20	5.26	15.78
S-11	317.00	95.29	15.57	71.04	149.45	166.46	108.12	5.18	609.04	7.21	15.96
S-10	260.96	90.99	15.61	57.56	134.65	95.43	128.16	5.75	581.13	7.71	13.71
S-9	186.86	81.47	12.66	59.73	113.43	167.04	64.77	4.43	453.09	11.68	17.07
S-8	197.61	61.21	11.40	62.52	106.65	185.66	94.00	5.63	434.76	11.05	18.76
S-7	366.46	86.46	11.16	70.81	121.55	168.65	73.32	2.99	471.99	8.77	18.56
S-6	238.42	63.10	16.94	65.27	81.84	183.13	68.54	8.79	377.76	16.85	16.02
S-5	388.01	52.74	11.45	69.40	89.24	184.94	62.59	8.65	375.20	11.37	14.91
S-4	198.55	35.86	9.16	45.57	79.33	196.97	46.36	6.93	408.63	9.11	12.94
S-3	117.76	60.70	14.74	59.18	93.27	143.50	71.05	10.90	450.60	15.12	17.95
S-2	190.44	40.24	11.73	76.62	84.09	111.33	62.06	10.07	477.03	12.40	13.75
S-1	3292.43	181.90	11.12	327.50	91.91	125.66	87.46	122.58	491.24	98.13	14.85
Mean	386.96	84.93	14.89	75.96	128.90	151.34	95.76	11.93	854.93	13.55	15.66
O-2	89.08	39.75	19.16	79.07	123.64	216.56	74.38	2.98	405.12	3.61	20.55
O-1	180.75	93.86	27.88	114.89	177.13	104.70	246.90	7.40	592.40	10.59	40.07
Mean	134.92	66.81	23.52	96.98	150.39	160.63	160.64	5.19	498.76	7.10	30.31

O_3w-S_1l_1 black shales are classified into three types of shale lithofacies: siliceous, clay shale, mixed shale, which further comprise seven subfacies. The dominant lithofacies is the mixed shale lithofaciess (M-7, 30%), followed by the clayey siliceous shale lithofacies (S-4, 20%) and the siliceous clay shale lithofacies (CM-2, 20%). The minor lithofacies include the calcium and clay siliceous shale lithofacies (S-3, 10%), the calcium clay siliceous mixed shale lithofacies (M-5, 10%), the calcium clay siliceous shale lithofacies (S-8, 5%), and the clay calcium siliceous mixed shale lithofacies (M-4, 5%) (Figure 2B; Table 6).

5 Discussion

5.1 Data validity analysis

5.1.1 Applicability of geochemical element evaluation index

In order to evaluate the likelihood of an event, this study utilizes significance tests from statistical theory to calculate the *p*-value among sedimentary geochemical parameters, as depicted in Figure 3. The RSEs, such as V, Mo, U, Ni and Cr, demonstrate variations in sedimentary rocks in response to different redox conditions. These elements are frequently utilized as indicators of paleoredox conditions within the sedimentary environment (Tribovillard et al., 2006). Multiple parameters are necessary to collectively constrain paleoenvironmental conditions and mitigate potential analytical errors in the determination of single-element concentrations (Qiu et al., 2021).

In this study, paleoredox conditions, represented by V/Cr, Ni/Co, and U/Th ratios, were utilized to confirm the correlations among sedimentary geochemical parameters. The resulting correlation coefficients were 0.96, 0.94, and 0.35, respectively. Furthermore, consistent explanatory outcomes observed across diverse paleoredox conditions in Section 5.3.1 offer additional support for the reliability of the data.

5.1.2 Late diagenesis

When performing a quantitative analysis of sedimentary geochemical characteristics in a paleoenvironment, it is crucial to recognize the complex composition of sediments in the source area, as well as the effects of potassium metasomatism and recycling during diagenesis on these characteristics (Gaillardet et al., 1999; Garzanti et al., 2013; Abedini and Calagari, 2017a; Perri, 2018).

The characteristics of REE content in clastic sedimentary rocks can be used as parameters to assess diagenetic intensity. Stronger

10.3389/feart.2023.1237495

TABLE 3 Content of rare earth elements (ug/g) in the O3w-S1l1 black shales.

Sample	La	Ce	Pr	Nd	Sm	Eu	Gd	Tb	Dy	Ho	Er	Tm	Yb	Lu
S-18	40.62	67.33	8.60	29.35	5.52	1.45	4.46	0.85	4.17	0.87	2.47	0.43	2.71	0.46
S-17	35.12	60.63	7.41	27.47	4.69	0.98	3.97	0.71	3.61	0.72	2.06	0.36	2.23	0.36
S-16	60.30	106.74	13.67	53.10	9.55	1.74	8.04	1.51	7.13	1.41	3.75	0.64	3.74	0.60
S-15	45.26	74.76	9.34	33.32	5.88	1.07	4.90	0.91	4.36	0.93	2.28	0.46	2.82	0.43
S-14	45.04	76.02	9.74	33.63	6.07	1.30	5.00	0.97	4.59	0.95	2.68	0.46	2.93	0.44
S-13	40.92	69.67	8.55	32.18	5.88	1.12	4.85	0.92	4.42	0.90	2.59	0.45	2.81	0.45
S-12	38.56	58.18	7.28	26.78	4.29	0.80	3.61	0.69	3.35	0.68	2.00	0.37	2.42	0.38
S-11	43.44	72.64	9.16	33.90	6.40	1.21	5.44	1.00	4.65	0.94	2.57	0.46	2.81	0.44
S-10	36.68	62.89	7.74	29.62	5.00	0.98	4.21	0.82	4.00	0.84	2.15	0.42	2.60	0.41
S-9	31.89	55.79	7.29	28.12	5.27	0.98	4.58	0.86	4.27	0.82	2.27	0.38	2.41	0.37
S-8	32.41	53.72	6.47	23.30	4.02	0.77	3.56	0.70	3.87	0.83	2.43	0.44	2.74	0.42
S-7	42.94	65.29	8.49	33.32	6.16	1.07	5.09	0.96	4.52	1.01	2.74	0.49	3.09	0.48
S-6	32.55	60.94	8.17	34.13	7.48	1.33	6.28	1.17	5.38	1.12	2.88	0.47	2.79	0.42
S-5	38.28	66.96	8.63	34.40	6.51	1.28	5.72	1.05	4.97	1.03	2.75	0.46	2.82	0.44
S-4	31.84	58.20	7.19	29.58	6.61	1.18	5.91	1.11	4.96	1.09	2.95	0.49	2.98	0.45
S-3	42.51	76.93	9.83	38.70	7.04	1.26	5.75	0.93	4.56	0.93	2.08	0.41	2.53	0.39
S-2	40.10	72.23	9.06	33.96	6.14	0.97	4.55	0.84	3.82	0.80	2.18	0.39	2.49	0.39
S-1	30.08	53.37	9.01	37.91	7.91	1.46	7.15	1.48	7.38	1.59	4.49	0.75	4.53	0.74
Mean	39.36	67.35	8.65	32.93	6.13	1.16	5.17	0.97	4.67	0.97	2.63	0.46	2.86	0.45
O-2	38.44	87.83	8.55	30.99	5.59	0.96	4.96	0.91	4.43	0.96	2.63	0.47	2.78	0.43
O-1	62.32	128.98	10.30	34.06	5.24	0.98	5.37	1.01	5.20	1.34	4.37	0.89	5.89	0.99
Mean	50.38	108.41	9.43	32.53	5.42	0.97	5.17	0.96	4.82	1.15	3.50	0.68	4.34	0.71

diagenesis is associated with a stronger correlation between δCe and ΣREE, as well as Dy_S/Sm_S (Shields and Stille, 2001). The δCe of O_3w-S_1l_1 black shales shows a weak correlation with Dy_S/Sm_S and ΣREE, indicating a limited influence of diagenesis on these elements (Figures 4A,B). Additionally, the comparison of the correlation between CIA, K-co CIA, and CIW suggests that potassium metasomatism has had a negligible impact on the O_3w-S_1l_1 black shales (Nesbitt and Young, 1984; Fedo et al., 1995; Zhang X. S. et al., 2017) (Figures 4C,D). The majority of black shale samples have ICV values greater than 1, ranging from 0.87 to 2.51, with an average value of 1.41, suggesting limited recycled sedimentation and low maturity of the clastic rock composition (Van De Kamp and Leake, 1985; Cox et al., 1995). These samples can be used to assess the paleoenvironmental in the study area.

5.2 Origin of silica

Previous studies have indicated that silica in sedimentary rocks primarily originates from three sources: siliceous organisms, hydrothermal fluids, and silica-rich terrigenous debris (Van Den Boorn et al., 2007). During the Early Silurian, the Yangtze foreland basin represented a paleoenvironment with an epicontinental sea, accompanied by frequent volcanic eruptions in multiple phases. As a result, a complex composition of siliceous genesis influenced by various factors emerged (Cai et al., 2022b; Lu et al., 2022). The Al/(Al+Fe+Mn) of Si_{bio} is usually >0.60, with a δEu value <1, whereas the Al/(Al+Fe+Mn) of hydrothermal silica is generally <0.30, with a δEu value >1 (Adachi et al., 1986; Murray, 1994; Khan et al., 2019). The Si/(Si+Al+Fe) of O_3w-S_1l_1 black shales in the study area ranges from 0.72 to 0.79 (avg. 0.76), and the δEu value ranges from 0.56 to 0.89 (avg. 0.63). Based on the ∑REE-Cu+Co+Ni, Th-U, Al/Al+Fe+Mn-LogFe/Ti, and Al_2O_3-Fe_2O_3-MnO plots (Figures 5A–D), the O_3w-S_1l_1 black shales are primarily associated with non-hydrothermal deposits, showing limited influence from seafloor hydrothermal deposition. These findings indicate that the siliceous component of O_3w-S_1l_1 is predominantly a typical biogenic deposit. Tuff layers, widely distributed in the Yangtze foreland basin during the O-S, are relatively thin, with an average thickness of 2–10 cm, and are interpreted as deposits transported from a distant source (Yang et al., 2022). Hence, these volcanic deposits cannot prove the existence of a heat source in the Yangtze foreland basin and surrounding areas but they suggest indicate a limited influence of volcanogenic silica on siliceous minerals (Wang et al., 2017).

10.3389/feart.2023.1237495

TABLE 4 Content of geochemical indexes in the O_3w-S_1l_1 black shales.

Sample	V_{EF}	Cr_{EF}	Co_{EF}	Ni_{EF}	Rb_{EF}	Sr_{EF}	Zr_{EF}	Mo_{EF}	U_{EF}	Th_{EF}
S-18	2.44	3.00	2.16	2.94	1.39	0.58	0.62	2.05	1.43	1.27
S-17	3.30	2.46	1.72	3.12	1.34	0.38	0.55	4.21	2.15	1.37
S-16	2.80	2.56	1.60	2.44	1.33	0.51	1.02	3.50	2.59	1.50
S-15	2.29	2.37	1.57	2.18	1.42	0.27	0.51	1.19	1.26	1.38
S-14	2.62	2.67	1.62	2.59	1.41	0.34	0.55	1.47	1.20	1.37
S-13	2.35	2.02	1.52	2.24	1.39	0.24	0.53	1.13	1.23	1.26
S-12	3.07	2.88	1.48	3.22	1.38	0.34	0.44	1.18	1.86	1.52
S-11	5.37	2.77	1.58	3.61	1.36	0.48	0.58	3.51	2.62	1.58
S-10	4.86	2.91	1.75	3.22	1.34	0.30	0.75	4.29	3.08	1.49
S-9	3.32	2.48	1.35	3.18	1.08	0.51	0.36	3.15	4.45	1.77
S-8	3.62	1.92	1.25	3.44	1.05	0.58	0.54	4.13	4.34	2.00
S-7	6.57	2.66	1.20	3.81	1.17	0.52	0.42	2.15	3.37	1.94
S-6	5.23	2.37	2.23	4.30	0.96	0.69	0.47	7.71	7.92	2.05
S-5	9.13	2.13	1.62	4.90	1.12	0.75	0.46	8.14	5.73	2.04
S-4	3.29	1.02	0.91	2.26	0.70	0.56	0.24	4.59	3.23	1.25
S-3	2.53	2.23	1.90	3.81	1.07	0.53	0.48	9.36	6.96	2.25
S-2	5.25	1.90	1.94	6.34	1.24	0.53	0.54	11.10	7.33	2.21
S-1	87.03	8.24	1.76	25.97	1.30	0.57	0.73	129.61	55.58	2.29
Mean	8.62	2.70	1.62	4.64	1.23	0.48	0.54	11.25	6.46	1.70
O-2	1.88	1.43	2.42	4.99	1.39	0.78	0.49	2.51	1.63	2.52
O-1	2.20	1.96	2.03	4.19	1.15	0.22	0.95	3.60	2.76	2.84
Mean	2.04	1.70	2.23	4.59	1.27	0.50	0.72	3.06	2.20	2.68
Sample	ΣREE	LREE	HREE	L/H	$(La/Yb)_N$	δEu	δCe	Ba_{bio}	CIA	Si_{xs}
S-18	169.29	152.87	16.42	9.31	10.11	0.89	0.87	3631.40	70.62	5.40
S-17	150.32	136.30	14.02	9.72	10.62	0.69	0.90	775.75	70.26	21.99
S-16	271.92	245.10	26.82	9.14	10.87	0.61	0.89	717.99	69.15	12.76
S-15	186.72	169.63	17.09	9.93	10.82	0.61	0.88	687.06	70.83	4.04
S-14	189.82	171.80	18.02	9.53	10.36	0.72	0.87	3152.64	70.91	1.94
S-13	175.71	158.32	17.39	9.10	9.82	0.64	0.90	688.47	70.79	4.72
S-12	149.39	135.89	13.50	10.07	10.74	0.62	0.84	604.08	70.17	15.23
S-11	185.06	166.75	18.31	9.11	10.42	0.63	0.88	608.92	69.56	10.92
S-10	158.36	142.91	15.45	9.25	9.51	0.65	0.90	581.02	69.71	26.67
S-9	145.30	129.34	15.96	8.10	8.92	0.61	0.88	452.98	70.42	−2.35
S-8	135.68	120.69	14.99	8.05	7.97	0.62	0.89	434.65	69.50	0.77
S-7	175.65	157.27	18.38	8.56	9.37	0.58	0.82	471.88	70.41	5.16
S-6	165.11	144.60	20.51	7.05	7.87	0.59	0.90	377.67	67.54	6.27
S-5	175.30	156.06	19.24	8.11	9.15	0.64	0.89	375.12	68.55	10.20
S-4	154.54	134.60	19.94	6.75	7.20	0.58	0.93	408.51	64.47	6.87

(Continued on following page)

TABLE 4 (*Continued*) Content of geochemical indexes in the O_3w-S_1l_1 black shales.

Sample	V_{EF}	Cr_{EF}	Co_{EF}	Ni_{EF}	Rb_{EF}	Sr_{EF}	Zr_{EF}	Mo_{EF}	U_{EF}	Th_{EF}
S-3	193.85	176.27	17.58	10.03	11.33	0.61	0.91	450.51	65.09	24.67
S-2	177.92	162.46	15.46	10.51	10.86	0.56	0.91	476.96	65.41	48.58
S-1	167.85	139.74	28.11	4.97	4.48	0.59	0.78	491.17	67.74	31.20
Mean	173.77	155.59	18.18	8.74	9.47	0.64	0.88	854.82	68.95	13.06
O-2	189.93	172.36	17.57	9.81	9.32	0.56	1.17	405.03	68.75	14.20
O-1	266.94	241.88	25.06	9.60	7.13	0.56	1.23	592.24	71.57	−11.90
Mean	228.44	207.12	21.32	9.71	8.23	0.56	1.20	498.64	70.16	1.15

TABLE 5 Content of organic geochemistry indicators in the O_3w-S_1l_1 black shales.

Sample	TOC (%)	T_{max} (°C)	S_1+S_2 (mg/g)	S	V	TI	Type	Rb (%)	Ro(%)			
									Jacob (1985)	Jacob (1989)	Feng and Chen (1988)	Liu and Shi (1994)
S-18	0.79	556.00	0.04	96.00	4.00	93.20	I	2.69	2.06	2.80	2.75	2.15
S-17	1.80	557.00	0.09	95.00	5.00	91.50	I	2.70	2.07	2.81	2.76	2.15
S-16	2.47	556.00	0.10	95.00	5.00	91.50	I	2.72	2.08	2.82	2.78	2.17
S-15	0.81	556.00	0.05	—	—	—	—	—	—	—	—	—
S-14	0.75	557.00	0.05	96.00	4.00	93.20	I	2.69	2.06	2.80	2.75	2.15
S-13	1.00	557.00	0.06	—	—	—	—	—	—	—	—	—
S-12	1.85	557.00	0.08	92.00	8.00	86.40	I	2.68	2.06	2.79	2.74	2.14
S-11	2.01	557.00	0.08	93.00	7.00	88.10	I	2.74	2.09	2.84	2.80	2.18
S-10	2.45	558.00	0.11	—	—	—	—	—	—	—	—	—
S-9	2.91	558.00	0.11	96.00	4.00	93.20	I	2.83	2.15	2.93	2.89	2.24
S-8	2.51	558.00	0.11	94.00	6.00	89.80	I	2.86	2.17	2.96	2.92	2.26
S-7	2.43	558.00	0.10	—	—	—	—	—	—	—	—	—
S-6	3.63	487.00	0.11	95.00	5.00	91.50	I	2.87	2.17	2.97	2.93	2.27
S-5	2.87	575.00	0.05	—	—	—	—	—	—	—	—	—
S-4	2.40	563.00	0.10	98.00	2.00	96.60	I	2.90	2.19	3.00	2.95	2.29
S-3	2.50	560.00	0.09	—	—	—	—	—	—	—	—	—
S-2	3.03	407.00	0.14				—	—	—	—	—	—
S-1	8.21	556.00	0.13	—	—	—	—	—	—	—	—	—
Mean	2.47	546.28	0.09	95.00	5.00	91.50	I	2.77	2.11	2.87	2.83	2.20
O-2	0.43	340.00	0.05	96.00	4.00	93.20	I	2.94	2.22	3.03	2.99	2.32
O-1	0.99	537.0	0.03	91.00	9.00	84.70	I	2.92	2.20	3.02	2.97	2.30
Mean	0.71	438.50	0.04	93.50	6.50	88.95	I	2.93	2.21	3.03	2.98	2.31

5.3 Reconstruction of paleoenvironment

5.3.1 Paleoredox conditions and paleoseawater restriction

Paleoredox conditions refer to the equilibrium between oxygen and reducing agents in the sedimentary environment, which significantly influence the type and preservation of OM. An elevated oxidant content accelerates the degradation of OM, while a high reducing agent content inhibits it (Zhang et al., 2016). Marine sedimentary environments are commonly reconstructed using RSEs in marine deposits, such as V, Cr, Th, U, and Mo, owing to their distinct behaviours under seawater

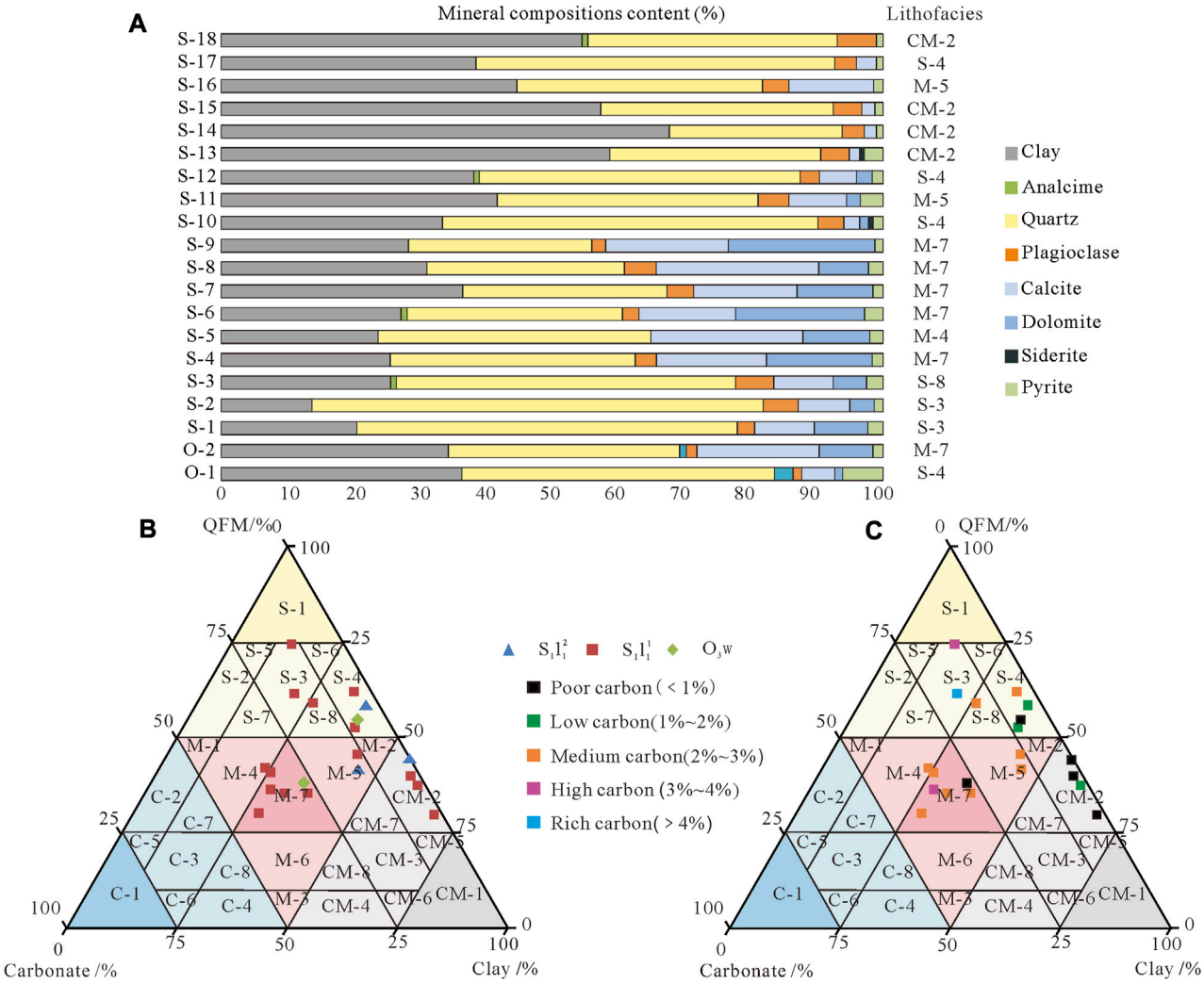

FIGURE 2
Lithological characteristics of O_3w-S_1l_1 black shales (Wang et al., 2018). **(A)** Vertical variations in mineral content and lithofacies types; **(B)** Distribution of lithofacies types in shale across various layers; **(C)** Distribution of lithofacies types in shale with varying TOC content.

oxidation-reduction conditions (Tribovillard et al., 2006; Algeo and Rowe, 2012; Scott and Lyons, 2012; Abedini et al., 2019). V is typically taken up by OM and becomes enriched in reducing environments. Sediments deposited in a low-oxygen environment exhibit high U values (Abedini and Calagari, 2017b).

The redox classifications (O_2 concentration in bottom waters, ml O_2/H_2O) in this research adhere to the standards established by Tyson and Pearson (1991), which include oxic: $[O_2]>2$, suboxic: $2>[O_2]>0.2$, anoxic(no free H_2S in the water column): $[O_2]<0.2$, and euxinic(free H_2S present in the water column): $[O_2]=0$. Hatch and Leventhal (1992), Jones and Manning (1994), and Wignall and Twitchett (1996) identified that V/Cr<2, Ni/Co<5, and U/Th<0.75 indicate an oxygen-rich environment, while V/Cr indicate 2-4.25, 5 <Ni/Co<7, and 0.75 <U/Th<1.25 indicate an oxygen-depleted suboxic-anoxic environment. Finally, V/Cr>4.25, Ni/Co>7, and U/Th>1.25 show a euxinic environment. Based on the results presented in Figures 6A–C, the O_3w black shales indicate an oxic-anoxic environment, while the S_1l1 1 black shales exhibit a strongly reducing sedimentary environment with a decreasing reduction trend vertically.

The retention of seawater in a basin has a significant impact on the enrichment and preservation of OM. OM in water is more likely to be enriched and preserved under conditions of slower water exchange and renewal (Algeo and Rowe, 2012). U_{EF}-Mo_{EF} and TOC-Mo are effective indicators of the oxygen conditions and the extent of sediment retention in the environment (Algeo and Tribovillard, 2009; Tribovillard et al., 2012). Mo/TOC can determine seawater retention degree under reducing paleoenvironmental conditions. Under euxinic environmental conditions, the degree of seawater retention can be determined using Mo/TOC, whereas, in oxic environments, the values of Mo and Mo/TOC are determined by the redox environment rather than the degree of seawater retention (Zheng et al., 2002; Algeo and Rowe, 2012; Li et al., 2015). The low TOC and Mo content in the O_3w black shales make it unsuitable for using Mo/TOC to determine its seawater retention degree. In contrast, the S_1l_1 black shales were deposited in

TABLE 6 Mineral composition (%) in O_3w-S_1l_1 black shales.

Sample	Lithofacies	TOC(%)	Clay	Anl	Qtz	Or	Pl	Cal	Dol	Sd	Py	Br(%)
S-18	CM-2	0.79	54.50	0.90	37.70	—	5.90	—	—	—	1.00	44.60
S-17	S-4	1.80	38.50	—	54.20	—	3.30	3.00	—	—	1.00	61.50
S-16	M-5	2.47	44.70	—	37.10	—	4.00	12.80	—	—	1.40	55.30
S-15	CM-2	0.81	57.40	—	35.20	—	4.30	2.00	—	—	1.20	42.66
S-14	CM-2	0.75	67.70	—	26.10	—	3.40	1.80	—	—	1.00	32.30
S-13	CM-2	1.00	58.70	—	31.90	—	4.30	1.60	—	0.70	2.80	41.30
S-12	S-4	1.85	38.20	0.80	48.60	—	2.90	5.60	2.40	—	1.60	61.04
S-11	M-5	2.01	41.70	—	39.40	—	4.70	8.70	2.10	—	3.40	58.30
S-10	S-4	2.45	33.40	—	56.80	—	3.90	2.40	1.30	0.70	1.50	66.60
S-9	M-7	2.91	28.30	—	27.70	—	2.10	18.50	22.20	—	1.20	71.70
S-8	M-7	2.51	31.10	—	29.90	—	4.80	24.60	7.50	—	2.20	68.93
S-7	M-7	2.43	36.50	—	30.90	—	4.00	15.60	11.50	—	1.50	63.50
S-6	M-7	3.63	27.20	0.90	32.60	—	2.50	14.60	19.50	—	2.80	71.93
S-5	M-4	2.87	23.70	—	41.20	—	—	23.00	10.10	—	2.00	76.30
S-4	M-7	2.40	25.50	—	37.00	—	3.20	16.60	16.00	—	1.60	74.47
S-3	S-8	2.50	25.60	0.90	51.30	—	5.80	9.00	5.00	—	2.50	73.53
S-2	S-3	3.03	13.70	—	68.10	—	5.30	7.80	3.70	—	1.30	86.29
S-1	S-3	8.21	20.50	—	57.50	—	2.60	9.00	8.10	—	2.30	79.50
Mean	—	2.47	37.05	0.88	41.29	—	3.94	10.39	9.12	0.70	1.79	62.76
O-2	M-7	0.43	34.30	—	34.90	1.00	1.60	18.50	8.10	—	1.50	65.67
O-1	S-4	0.99	36.40	—	47.30	2.80	1.30	5.00	1.20	—	6.10	63.64
Mean	—	0.71	35.35	—	41.10	1.90	1.45	11.75	4.65	—	3.80	64.66

Note: Anl represents; Qtz represents Quartz; Or represents Orthoclase; Pl represents Plagioclase; Cal represents Calcite; Dol represents Dolomite; Sd represents Siderite; Py represents Pyrite.

an anoxic-euxinic environment with high seawater retention (Figures 5E,F).

Upwelling sediments tend to have higher enrichment of Cd and Mo, while Co and Mn are relatively depleted. Co×Mn<0.4, Co_{EF}×Mn_{EF}<0.5, and Cd/Mo>0.1 are characteristic indicators of upwelling sediments. Stronger upwelling activity corresponds to lower values of Co×Mn or Co_{EF}×Mn_{EF} in the sediment and higher Cd/Mo ratios. Sediments in seasonal upwelling environments typically exhibit Cd/Mo ratios ranging from 0.1 to 0.6, while sediments in perennial upwelling environments have Cd/Mo ratios >0.6 (Crusius et al., 1996; Algeo and Tribovillard, 2009; Nakagawa et al., 2012; Scott and Lyons, 2012; Sweere et al., 2016). Figures 5G–I and Figure 6D illustrate the enhanced retention of O_3w black shales during its sedimentation period, while S_1l_1 black shales were subjected to seasonal upwelling influences.

During the Hirnantian stage (late Ordovician), the cold climate and expanding ice cover may have led to the emergence of high paleo-topography (Zigong uplift) above sea level. As a result, the accommodation space and relative paleoseawater depth of the Weiyuan area may have been affected. The periodic closure of the environment resulted in interrupted exchange between the basin and seawater, leading to a weaker upwelling intensity as indicated by the geochemical elements (Wang et al., 2018; Liang et al., 2019; Qiu et al., 2020b). In contrast, the relatively high sea level during the Rhuddanian stage (early Silurian) promoted seawater exchange and nutrient supply between the basin and the vast oceanic currents (Haq and Schutter, 2008; Cai et al., 2022a).

5.3.2 Paleoproductivity

Paleoproductivity refers to the primary productivity of paleoseawater ecosystems during a geological period, encompassing plant and phytoplanktonic primary productivity, among others (Tribovillard et al., 2006; Wei, H., 2012). Barium (Ba) is a well-established element utilized as an indicator of paleoproductivity (Wedepohl, 1971). The average Ba_{bio} content in the O_3w-S_1l_1 black shales of the Yangtze foreland basin is 497.79 μg/g and 683.40 μg/g, respectively. Notably, the Ba_{bio} content of high TOC samples in the S_1l_1 black shales are significantly lower than that of other samples, suggesting reduced overall productivity (Figure 6F). This is due to the decomposition of barite (the primary occurrence form of Ba by sulfur-reducing bacteria and other microorganisms through bacterial sulfate reduction (BSR) in a relatively restricted environment, leading to a relatively low Ba_{bio}

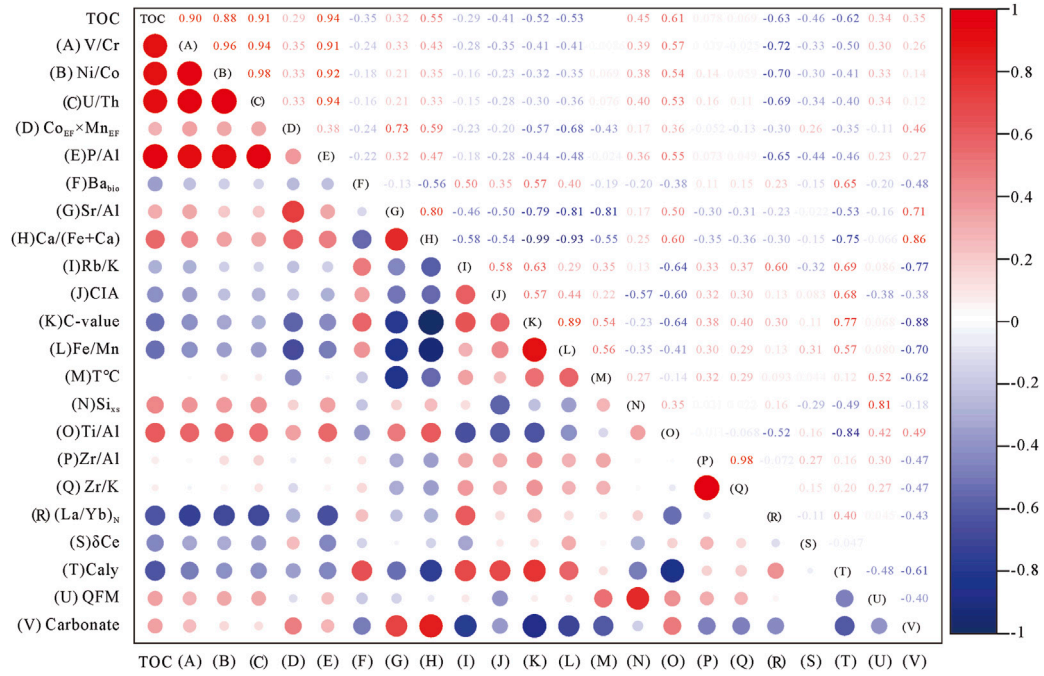

FIGURE 3
The correlation coefficient of paleoenvironmental geochemical indicators. Red circles indicate a positive correlation, and blue circles indicate a negative correlation. Darker colours indicate a stronger correlation.

content in organic-rich black shales. Consequently, employing Ba as an indicator of productivity, may produce distorted results, and relatively low Ba_{bio} content does not necessarily signify low levels of paleoproductivity during the deposition of the O_3w-S_1l_1 black shales (Dymond et al., 1992; Murray and Leinen, 1993; Yan et al., 2015). Previous studies have demonstrated that the biogenic component Si_{bio} (Si_{xs}) is a valuable parameter for estimating paleoseawater productivity (Tribovillard et al., 2006; Khan et al., 2019). According to Chapter 5.2, the siliceous content in the O_3w-S_1l_1 black shales are primarily biogenic, which can be used to evaluate paleoproductivity. The vertical variation of Si_{xs} content in the O_3w-S_1l_1 black shales suggests a higher paleoproductivity level for the S_1l_1 shales than the O_3w shales.

Wang et al. (2002) reported that the Hirnantia fauna thrived as a result of increased seawater oxygen content in the Yangtze Block. Rong and Huang, 2019 proposed that the Yangtze Block was located in the equatorial-tropical zone during the Late Ordovician and experienced minimal impact from the Gondwana glaciation. As a result, although the biological extinction rate was high, the ecological impact was minimal, and the level of paleoproductivity remained stable. The Zigong uplift in the Weiyuan area restricted the nutrient supply from upwelling. Additionally, the decline in global sea levels during the Hirnantian glacial epoch led to an elevation in oxygen content within the stratified water column. These changes resulted in an unfavourable sedimentary environment for preserving OM during the Late Ordovician (Wang et al., 2018). In the Early Silurian, the Yangtze foreland basin obtained nutrient supply from the open ocean, such as the Qinling Ocean to the north (Wang et al., 2017). Seasonal upwelling had a significant impact on seawater exchange and nutrient supply, consequently affecting paleoproductivity. Planktonic organisms, such as radiolarians and sponge spicules, exhibited their highest paleoproductivity levels during the Early Silurian (Figures 6E–G). The paleoproductivity levels of the O_3w-S_1l_1 black shales in the Weiyuan area exhibit substantial variations, primarily attributed to the influence of the regional oceanic environment and nutrient supply (Guo, 2017).

5.3.3 Paleoclimate and paleosalinity

Paleoclimate and paleosalinity conditions exert a significant influence on the provenance, abundance, and type of OM. Humid climate conditions may increase the deposition of OM, while high salinity water bodies can preserve it (Jin et al., 2008). The abundance of specific major and trace elements in shale, such as the CIA, C-value, and Fe/Mn ratios, can serve as indicators of paleoclimate conditions (Nesbitt and Young, 1982; Wang et al., 1997; Getaneh, 2002). Elevated Fe/Mn ratios in sediment are indicative of warm and humid climatic conditions, whereas low ratios suggest a hot and arid environment (Wang et al., 1997).

The CIA and K-co CIA values suggest that the O_3w-S_1l_1 black shales in the Yangtze foreland basin were deposited during warm and humid paleoclimatic conditions (Figures 5J,K; Figue 6J). The C-value and Fe/Mn trends suggest that the O_3w-S_1l_1 black shales experienced a shift in climatic conditions from humid to dry and then back to humid during the deposition process (Figures 6K,L). The paleosalinity indicators, Ca/(Fe+Ca) and Rb/K in Figures 6H–I, indicate that seawater salinity increased during the late Ordovician because of global climate change and the stagnant water habitat in the basin. In contrast, during the early Silurian, water circulation increased as the glacial epoch ended, reducing seawater salinity. Dong et al. (2022) states that this

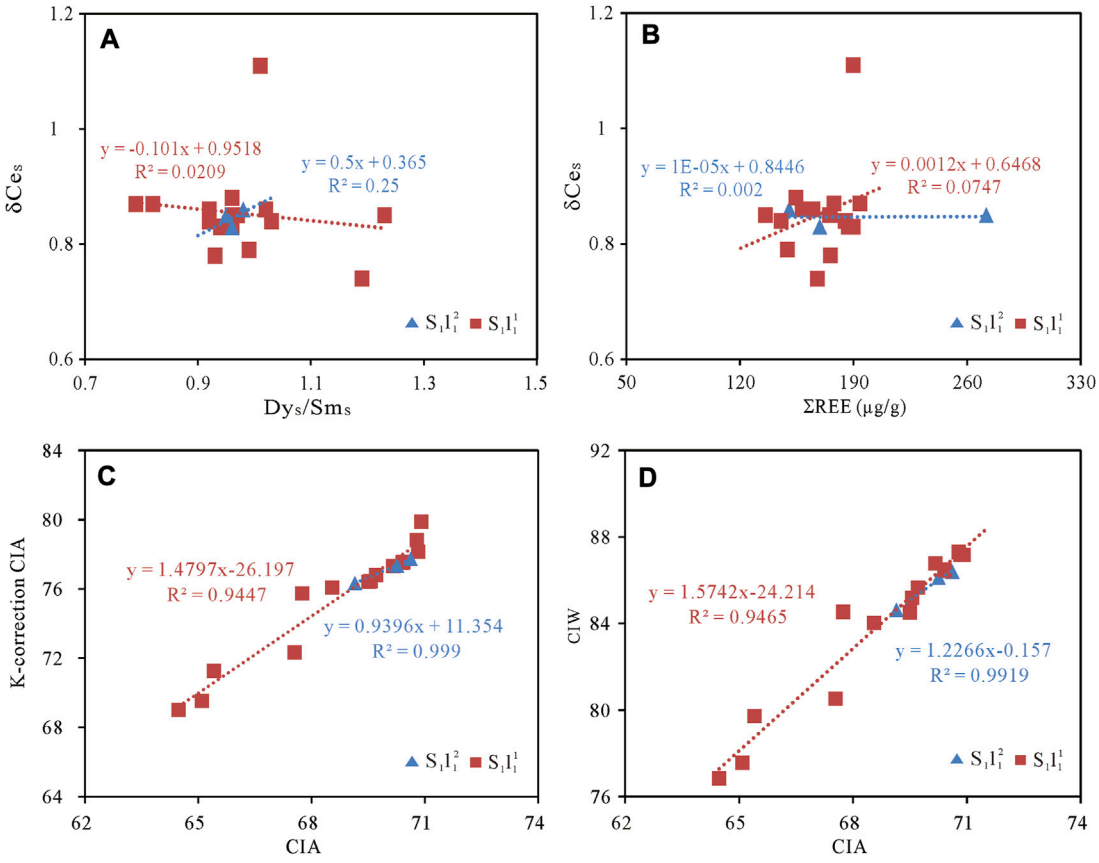

FIGURE 4
Indicator for late diagenesis. **(A)** Dy_S/Sm_S-δCe; **(B)** ΣREE-δCe; **(C)** CIA-Correction CIA; **(D)** CIA-CIW.

change is attributed to regional climate conditions and the oceanic environment in the Yangtze foreland basin during the early Silurian.

5.3.4 Paleoseawater temperature

During the Early to Late Ordovician, the South China Plate migrated northward from the subtropical climate zone to the tropical climate zone near the equator, resembling the modern-day Galápagos Islands in Ecuador(Figure 7) (Torsvik and Cocks, 2013). This northward migration was expected to lead to higher paleoseawater temperature. However, evidence from stable oxygen isotope data of conodonts and apatites indicates that the South China Plate underwent a transition from warm to cold water during the Early to Late Ordovician, contradicting the results of paleogeographic reconstructions (Jin et al., 2018). The Sr element estimation of paleoseawater temperature in the Yangtze foreland basin during the O-S interval ranged from 10.64°C to 26.08°C (17.92°C). This value is considerably lower than the average equatorial temperature of 27°C recorded during that period (Figure 6M). The substantial global temperature decrease of approximately 9°C observed during the same period could account for the apparent contradiction and imply that the Hirnantian glacial event might have impacted the marine environment of the Yangtze foreland basin (Melchin et al., 2013).

5.3.5 Terrigenous detrital input

Terrigenous detrital input particularly impacts sedimentary environments, as it can enrich sediment with nutrients and dilute the abundance of OM. Al and Ti serve as reliable indicators for assessing the intensity of terrigenous detrital input, as they are minimally affected by weathering and diagenesis, thereby preserving the signature of the source region (Nesbitt et al., 1996). A strong correlation between Al and Ti, Th, Nb, Zr, or Hf indicates that Al is derived from typical silicate detrital input (Tribovillard et al., 2006; Tribovillard et al., 2012). Ti/Al and Zr/Al ratios provide insights into the intensity of terrigenous detrital input.

The elevated Ti/Al and Zr/Al ratios observed during the $S_1l_1^1$ in comparison to the O_3w (Figures 6O, P) indicate a relatively more significant input of terrigenous detritus in the Yangtze foreland basin during this period. This can be attributed to the intensified tectonic activity (Guangxi movement), which supplied a substantial detrital input starting from the late O_3w. Furthermore, the sea level decrease during the Hennantian glaciation led to the exposure and weathering of certain portions of the original seafloor material. Subsequently, these materials were transported to the seabed after the glaciation, resulting in a comparatively higher input of detrital material during this period. Following the sea level rise to a certain threshold, the water environment stabilizes, leading to a gradual decline in the terrigenous detritus (Ti/Al) content, albeit the change

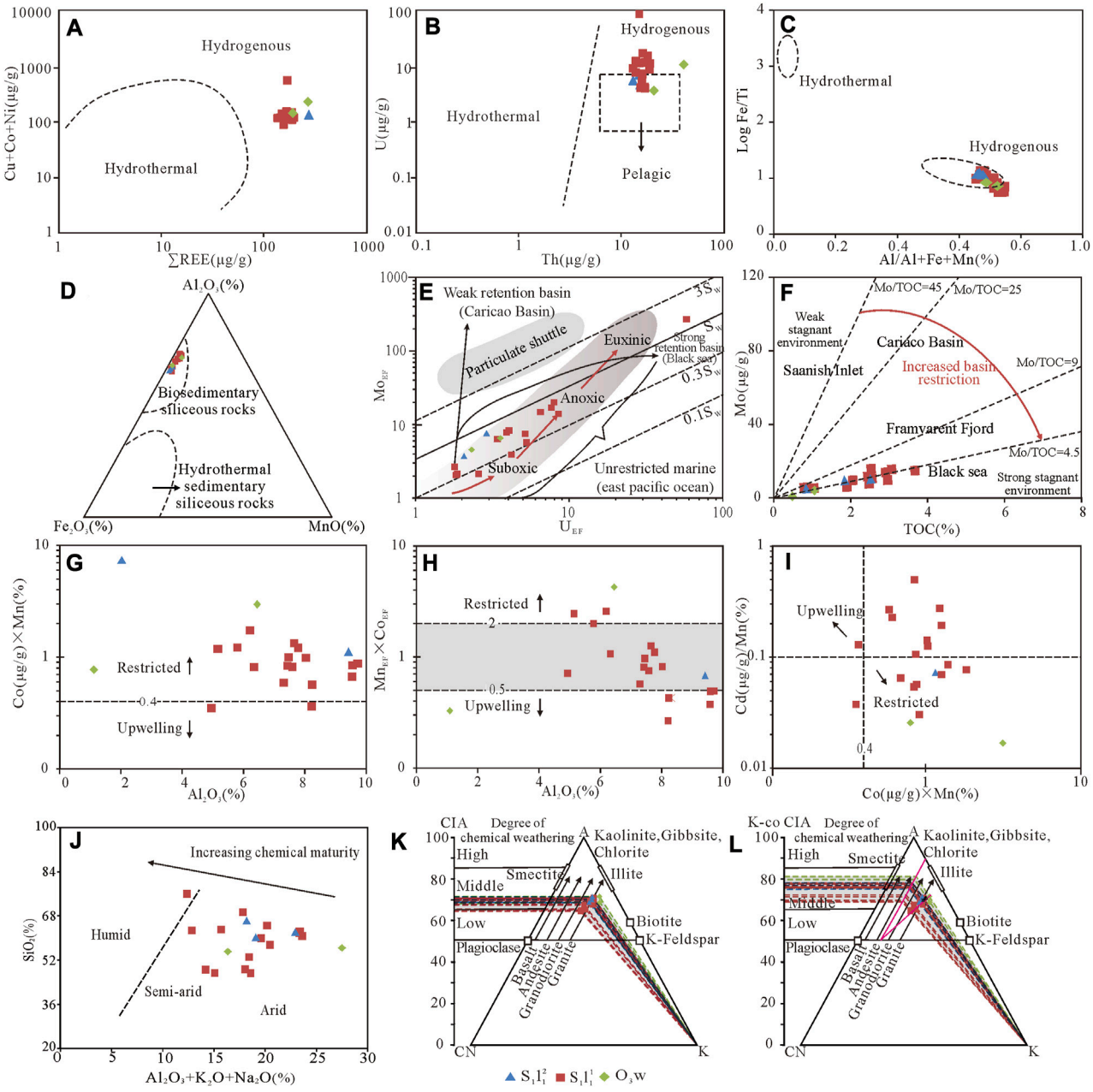

FIGURE 5
Discrimination chart of the paleoenvironmental geochemical index in the Yangtze foreland basin from Late Ordovician to Early Silurian. Plates **A-D** show origin of sillica, **E-I** show paleoredox conditions and seawater restriction, **J-L** show paleoclimate.

is not significant in its entirety. During the $S_1l_1^2$, a global decrease in sea level occurred, resulting in an upward trend in Ti/Al ratios, signifying an augmentation in the input of terrigenous detritus.

Moreover, the variation in shale lithofacies indicates alterations in the intensity of terrigenous detritus input. Chapter 4.3 demonstrates that the lowermost portion in S_1l_1 comprises siliceous shale, which gradually transitions vertically to mixed shale and clay shale with a higher clay mineral content. This vertical change signifies an augmentation in the intensity of terrigenous detrital input.

5.3.6 Sedimentation rate

The sedimentation rate (SR) notably impacts the preservation duration and type of OM (Ding et al., 2021; Khaled et al., 2022). In marine sedimentary environments, sediment rich in OM tends to accumulate in areas with low oxygen levels and slow SR (Wignall and Twitchett, 1996; Schulte et al., 2000; Chen et al., 2006). According to Ibach (1982), an increase in SR can enhance the burial efficiency of OM when the SR of black shale falls below 3.2 m/Myr. Differential sediment particle SR induces REE fractionation (Murray et al., 1991). Under slow SR, REE are

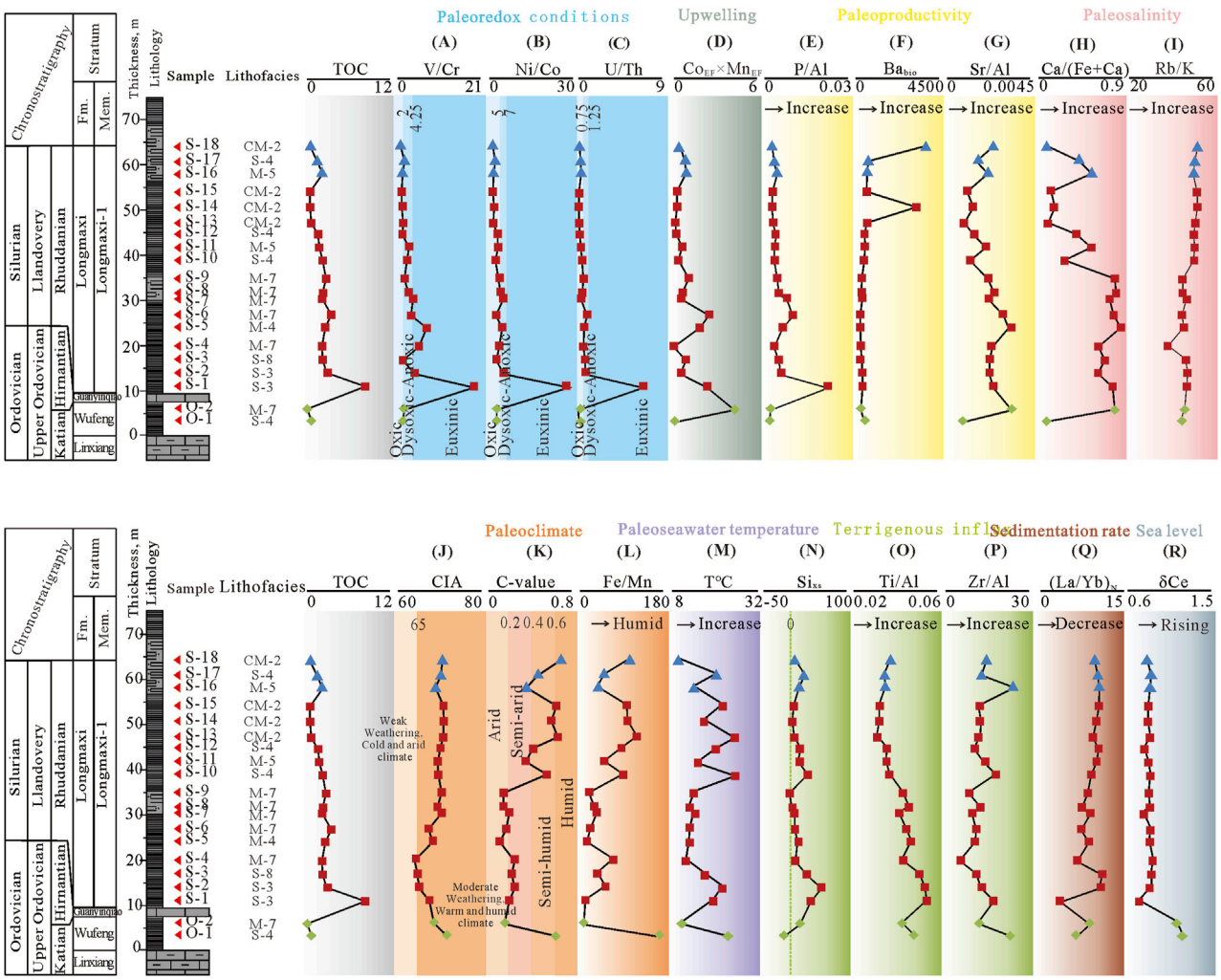

FIGURE 6
Vertical variation of the paleoenvironmental geochemical index in the Yangtze foreland basin from Late Ordovician to Early Silurian. Plates **A-C** show paleoredox conditions, **D** shows upwelling, **E-G** show paleoproductivity, **H-I** show paleosalinity, **J-L** show paleoclimate, **M** shows paleoseawater temperature, **N-P** show terrigenous influx, **Q** shows sedimentation rate and **R** shows sea level.

adsorbed by clay, complexed with OM, and subjected to pertinent chemical reactions. This process leads to the depletion (or enrichment) of light (or heavy) REE, resulting in significant shift in the $(La/Yb)_N$ (with N representing the chondrite-normalized parameter). An approaching $(La/Yb)_N$ of 1 indicates minimal or weak fractionation of REE, implying a higher SR. Conversely, substantial deviation from 1 signifies notable REE fractionation, suggesting reduced SR (Elderfield and Greaves, 1982). The $(La/Yb)_N$ for the O_3w-S_1l_1 black shales are S_1l_1 (4.48–11.33, avg. 9.47)>O_3w (7.13–9.32, avg. 8.23), suggesting SR is lower for S_1l_1 than O_3w (Table 4; Figure 6Q). Guan (2020) calculated average SR in the graptolite zone in the Yangtze foreland basin: LM4 was 6.78 m/Myr; LM1-LM3 was 1.5 m/Myr; WF2-WF4 is 2.67 m/Myr, which is similar to the result of $(La/Yb)_N$ indication in this paper.

Variations in SR are closely linked to the paleogeographic conditions of the era, with a stable tectonic setting being a crucial factor for the low SR development (Zhang et al., 2005; Li et al., 2021). From the late Katian to Early Rhuddanian, the Yangtze foreland ramp experienced relatively minor and later tectonic influence from the southeastern margin of the Yangtze Block (Cathaysia orogenic belt). More substantial influence emerged during the Telychian (Llandovery, Silurian) due to heightened orogenic activity in the southeast (He, 2022; Zhao et al., 2023). The foreland ramp, distanced from uplifting and erosional regions, has slow SR, favoring OM enrichment and preservation. The black shales with high TOC content at the base of S_1l_1 was deposited in an environment with relatively high SR (Sample S-1, $(La/Yb)_N$=4.48, TOC=8.21%). OM may have been quickly buried after early diagenesis, efficiently bypassing regions with intense degradation during sedimentation. This likely contributed to a higher proportion of preserved OM (Zhang et al., 2023).

5.3.7 Sea level change

The δCe values in the black shales of O_3w-S_1l_1 range from 0.78 to 1.17. The presence of a substantial negative δCe anomaly in the black shales at the bottom of S_1l_1 indicates a significant sea level drop during this period, reaching its lowest point compared to the reference plane. This drop corresponds to the Hirnantian glacial

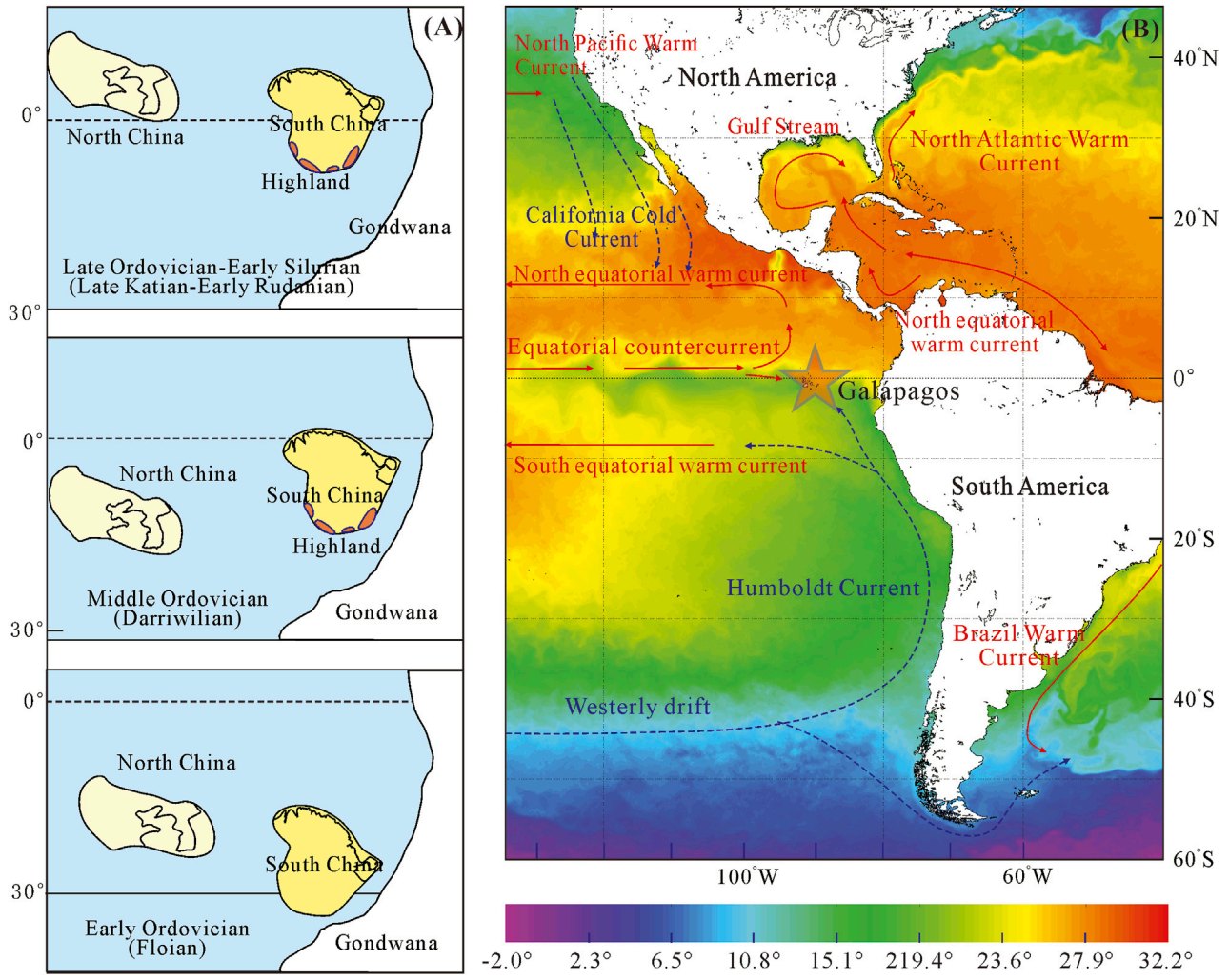

FIGURE 7
(A) Paleogeographic map of the South China Plate in Ordovician (Torsvik and Cocks, 2013; Jin et al., 2018); **(B)** Sea surface temperature chart around the modern equator. Data are from the National Oceanic and Atmospheric Administration: http://www.ospo.noaa.gov/Products/ocean/sst.html.

event that took place during the O-S (Figure 6R). The development of the Antarctic Gondwana ice sheet resulted in a swift and substantial global sea level decrease of approximately 100 m over a brief interval (Rong, 1984; Chen et al., 2001; Zhu et al., 2021). After the glacial period ended, the global sea level experienced frequent fluctuations. Nevertheless, the δCe value gradually increased and maintained stability within the range of 0.78–0.91. This pattern indicates a contemporaneous rise in sea level that aligns with trend depicted by the previously established global sea level curve (Liu et al., 2017). However, in the early Silurian, the regional Guangxi movement restricted the Yangtze Sea, impacting the water depth of the Yangtze Block due to the influence of surrounding uplifts. The magnitude of sea level rise was smaller than the uplift magnitude of the Zigong underwater highlands, resulting in a gradual or delayed increase in relative sea level (Li et al., 2023). The rise in relative sea level decreases the mixing efficiency in the water column, ultimately promoting the accumulation and preservation of OM in oxygen-depleted bottom water conditions. Additionally, this phenomenon creates more space for the burial of OM (Peng, 2021).

5.4 Controlling factors and enrichment mechanisms of OM

5.4.1 Lithofacies types influencing OME

Considering the influence of lithofacies types on TOC, the TOC content is classified into five groups based on the respective reference values: lean carbon (<1%), low carbon (1%–2%), medium carbon (2%–3%), high carbon (3%–4%), and rich carbon (>4%) (Wu et al., 2020). Organic-rich shale with TOC content exceeding 2% consists primarily composed of mixed shale (M-4, M-5, M-7) and siliceous shale (S-3, S-4, S-8) lithofacies (Figure 2C). These two shale lithofacies dominate primary gas-bearing interval of O_3w-S_1l_1, spanning from O-1 to S-12. The lithofacies thickness ratio between them is approximately 67.99% (41.17 m).

Commonly used proxies, such as quartz, QFM, SiO_2, and Si_{xs} (Si_{bio}), reflect silicon content characteristics in shale (Cai et al., 2020; Zhang et al., 2022). However, the correlation between silica content and TOC is nonlinear (Qiu et al., 2020a). Previous studies have

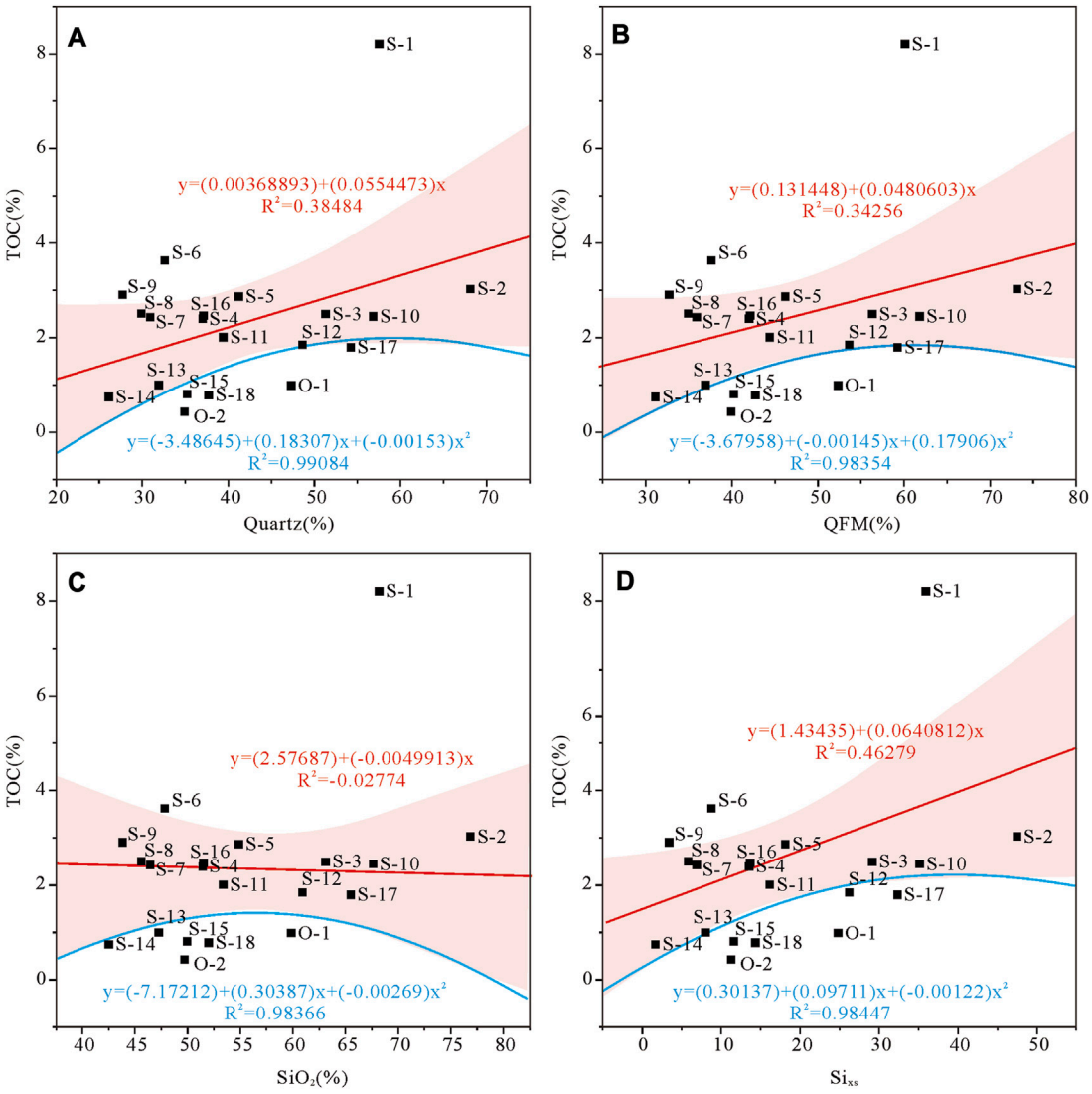

FIGURE 8
Correlation analysis between indicators of siliceous content (quartz, QFM, SiO_2, Si_{xs}) and TOC. The red line and equation indicate a linear relationship, and the red band represents the linear equation's confidence interval. Both correlation coefficients between TOC and siliceous content are less than 0.5, demonstrating either a weak negative correlation or no correlation with siliceous content. The blue line and equation indicate a nonlinear relationship, displaying a high degree of correlation between TOC and siliceous content and possessing characteristics of a standard distribution curve. This implies that the corresponding OM reaches its optimum state only when the siliceous content within the rock falls within a specific range rather than displaying a simple positive linear relationship.

demonstrated that shale reaches its highest TOC content when a specific balance between terrigenous silicon and biogenic silicon (Si_{bio}, Si_{xs}) is achieved. However, exceeding a threshold for Si_{xs} content leads to dilution and disaggregation effects that reduce TOC conten (Qiu et al., 2020a; Cai et al., 2020). Based on findings presented in Figure 8, the highest TOC content is reached when the quartz, QFM, and SiO_2 content around 55%, or when the proportion of Si_{xs} is approximately 30%.

5.4.2 The paleoenvironment influencing OME

Mechanisms influencing OME in marine sediments encompass diverse factors, classified into productivity and preservation mechanisms (Demaison, 1980; Pedersen. and Calvert, 1990; Murphy et al., 2000). The productivity mechanism underscores the pivotal role of primary productivity, proposing that heightened primary productivity and sufficient nutrient availability elevate oxygen consumption in the water column. Consequently, this fosters anoxic conditions, culminating in OME. Stated differently, anoxic bottom water conditions ensue as an outcome, not a cause, of OME (Pedersen. and Calvert, 1990; Sageman et al., 2003; Gallego Torres et al., 2007). The preservation mechanism indicates that anoxic water bodies formed in restricted basins can preserve OM.

TOC serves as a representative parameter to assess the extent of OME (Ma et al., 2018; Qiu et al., 2020a). We explore the correlation between TOC and eight sedimentary paleoenvironmental conditions, encompassing paleoredox conditions, paleoproductivity, paleoclimate, paleosalinity, paleowater

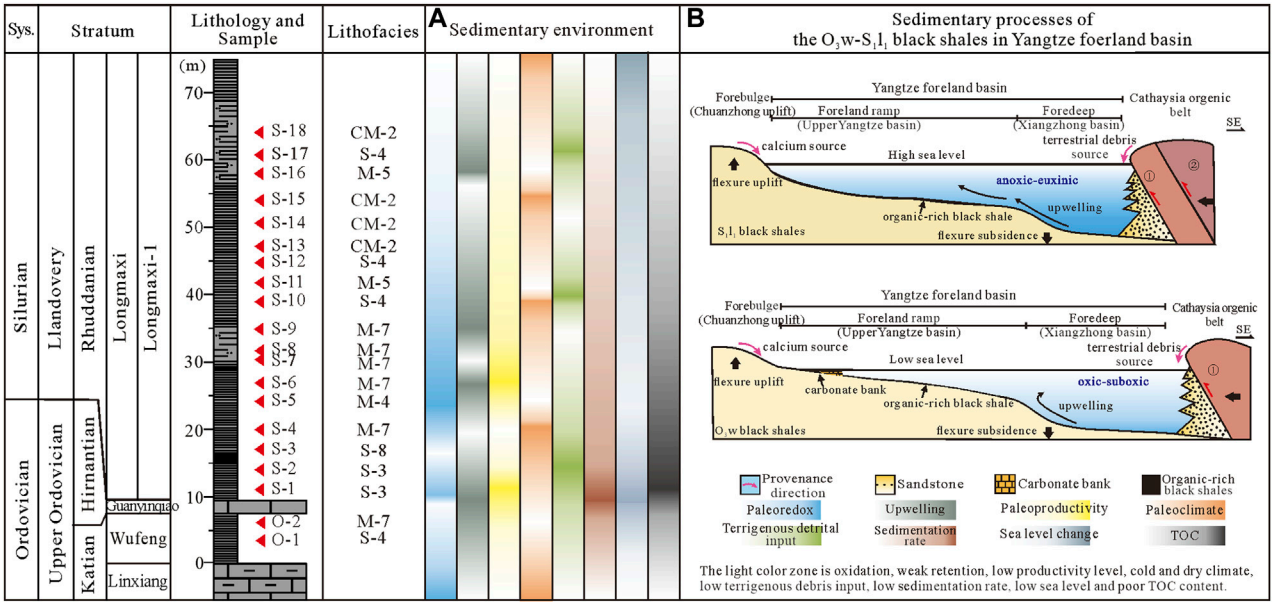

FIGURE 9
Organic matter enrichment mechanisms of the Upper Ordovician-Lower Silurian organic-rich black shales in the Yangtze foreland basin. **(A)** The sedimentary environment of the O_3w-S_1l_1 black shales; **(B)** The sedimentary processes of the O_3w-S_1l_1 black shales.

temperature, terrigenous detrital input, sedimentation rate, and sea level change. Correlation analysis reveals the most substantial impact on OME by paleoredox conditions (e.g., V/Cr, Ni/Co) and paleoproductivity indicators (e.g., P/Al, Ba_{bio}), demonstrating positive correlations with TOC. Close behind are the paleosalinity indicators (e.g., Rb/K). Conversely, paleoclimatic conditions (e.g., CIA, C -value), the degree of terrigenous detrital input (e.g., Si_{xs}, Ti/Al), and sedimentation rate ($(La/Yb)_N$) show negative correlations with OME. In essence, a heightened OME concentration corresponds to reduced humid climate, terrigenous detrital input, and a relatively high SR (Figure 3). Overall, the OME observed in O_3w-S_1l_1 black shales from the Yangtze foreland basin reflects the influence of numerous factors. Thus, relying solely on individual mechanisms such as the productivity mechanism or preservation mechanism proves insufficient in comprehensively elucidating the enrichment and preservation of OM in black shales (Khaled et al., 2022; Li et al., 2022; Hu et al., 2023; Xu et al., 2023).

5.4.3 Mechanism of OME

The tectonic-sedimentary evolution of the early Paleozoic Yangtze foreland basin divided in two stages, each marked by subordinate tectonic loading: the Katian stage and the Rhuddanian stage (Su et al., 2007; Zhang et al., 2020). O_3w and S_1l_1, representative of two distinct sets of black shales, emerge as products of disparate tectonic movements, revealing varying paleogeographic origins (Ge et al., 2021). By assimilating the aforementioned paleoenvironmental geochemical indicators and regional geological context, we can summarize an OME mechanism for O_3w and S_1l_1 black shales within the Yangtze foreland basin (Figure 9).

During the late Katian, the development of the Gondwana ice sheet triggered a worldwide decline in sea levels, isolating the Yangtze foreland basin from the Yangtze Sea and impeding upwelling (Delabroye and Vecoli, 2010; Elrick et al., 2013; Algeo et al., 2016; Lu et al., 2019). Amidst the interplay of global sea level fluctuations and regional tectonic shifts (Guangxi movement), the Yangtze foreland basin transformed, fostering a seawater setting characterized by retention and high oxygen content (oxic) (Yan et al., 2009). Despite the flourishing of the Hirnantian fauna within the global cold water environment (Wang et al., 2002; Rong and Huang, 2019), the preservation of OM encountered hindrances within the oxic paleoenvironment.

During the Early Rhuddanian, a shift from a cold and arid to a warm and humid climate triggered the rapid melting of glaciers. The glacial meltwater substantially surged sea levels and relatively high SR (Haq and Schutter, 2008; Munnecke et al., 2010). Nevertheless, the continued compression associated with the Guangxi movement brought about a delayed or gradual relative sea-level rise for the Yangtze foreland basin (Li et al., 2023). These rising sea levels fostered euxinic conditions conducive to OM preservation. Furthermore, the Yangtze foreland basin experienced reduced terrestrial detrital input and diminished OM dilution compared to the source region (Cathaysia orogenic belt), augmenting OME (Zhao et al., 2023). Consequently, the OME observed in S_1l_1 black shales of the Yangtze foreland basin is rooted in regional tectonic dynamics and climatic factors. Subsequently, during the late Rhuddanian, the ongoing uplift of the forebulge brought about shallowing of the seawater on the foreland ramp. This period had a substantial volume of terrigenous coarse debris, disrupting the anoxic bottom environment. Consequently, the preservation conditions essential for OME deteriorated, leading to the dilution of OM abundance and a decline in TOC content.

6 Conclusion

Through our investigation of the organic geochemical characteristics, mineral composition, and sedimentary geochemical characteristics of the O_3w-S_1l_1 black shales in the Yangtze foreland basin, we have able to analyze the siliceous genesis, reconstruct the paleoenvironment, and examine the organic matter enrichment (OME) mechanism in the black shales. It provides valuable information for exploring and developing shale gas in the O_3w-S_1l_1 under different sedimentary locations. Our findings suggest that:

(1) The O_3w-S_1l_1 black shales exhibit a TOC content ranging from 0.43% to 8.21% and possess a sapropelic kerogen type (type I). The Ro values and T_{max} suggest that the shales have undergone the high-over mature stage, with a primary occurrence in the over-mature stage.
(2) The mineral composition of O_3w-S_1l_1 black shales reveals the identification of seven lithofacies: mixed shale lithofacies (M-7), clayey siliceous shale lithofacies (S-4), siliceous clay shale lithofacies (CM-2), calcium and clay siliceous shale lithofacies (S-3), calcium clay siliceous mixed shale lithofacies (M-5), calcium clay siliceous shale lithofacies (S-8), and clay calcium siliceous mixed shale lithofacies (M-4). The organic-rich shale, characterized by TOC >2%, is primarily found within the mixed shale lithofacies (M-4, M-5, M-7) and siliceous shale lithofacies (S-3, S-4, S-8).
(3) Biogenic silica (Si_{xs}, Si_{bio}) serves as the primary source of high silicon content in O_3w-S_1l_1 black shales. The highest TOC content is observed when Si_{xs} constitutes approximately 30% of the total silica content.
(4) The correlation between TOC content and paleoenvironment indicators reveals that the OME in O_3w-S_1l_1 black shales are controlled by regional tectonic movements and sea level changes. These changes result from the combined outcome of four essential factors: paleoredox conditions, paleoproductivity, paleoclimate, terrigenous detrital input and sedimentation rate. The Zigong Uplift may have a certain influence on the OME and shale gas accumulation potential in the Yangtze foreland basin.
(5) Despite the high level of paleoproductivity during the Late Ordovician, the oxygen-rich seawater conditions in the Yangtze foreland basin resulting from the global sea level decline were unfavourable for OME. Subsequently, during the early Rhuddanian period, a thick layer of organic-rich black shales were deposited in a relatively enclosed and reduced paleoenvironment. During the late Rhuddanian period, tectonic uplift disrupted the anoxic seawater conditions, resulting in a dilution of OM abundance due to an increase in terrigenous debris input.

Data availability statement

The original contributions presented in the study are included in the article/supplementary material, further inquiries can be directed to the corresponding author.

Author contributions

LZ formulated the research question and drafted the manuscript. YL contributed to the methodology. LZ and SZ conducted the statistical analysis. CZ supervised and edited the manuscript. CW was responsible for proofreading and editing the manuscript for grammar. All authors contributed to the article and approved the submitted version.

Conflict of interest

The authors declare that the research was conducted in the absence of any commercial or financial relationships that could be construed as a potential conflict of interest.

Publisher's note

References

Abedini, A., and Calagari, A. (2017b). Geochemistry of claystones of the Ruteh formation, NW Iran: implications for provenance, source-area weathering, and paleo-redox conditions. *njma* 194, 107–123. doi:10.1127/njma/2017/0040

Abedini, A., and Calagari, A. (2017a). REEs geochemical characteristics of lower cambrian phosphatic rocks in the gorgan-rasht zone, northern Iran: implications for diagenetic effects and depositional conditions. *J. Afr. Earth Sci.* 135, 115–124. doi:10.1016/j.jafrearsci.2017.08.018

Abedini, A., Rezaei Azizi, M., and Dill, H. (2019). Formation mechanisms of lanthanide tetrad effect in limestones: an example from arbanos district, NW Iran. *Carbonates Evaporites* 35, 1. doi:10.1007/s13146-019-00533-z

Adachi, M., Yamamoto, K., and Sugisaki, R. (1986). Hydrothermal chert and associated siliceous rocks from the northern Pacific their geological significance as indication od ocean ridge activity. *Sediment. Geol.* 47, 125–148. doi:10.1016/0037-0738(86)90075-8

Algeo, T., Marenco, P., and Saltzman, M. (2016). Co-Evolution of oceans, climate, and the biosphere during the 'ordovician Revolution': A review. *Palaeogeogr. Palaeoclimatol. Palaeoecol.* 458, 1–11. doi:10.1016/j.palaeo.2016.05.015

Algeo, T., and Rowe, H. (2012). Paleoceanographic applications of trace-metal concentration data. *Chem. Geol.* 324-325, 6–18. doi:10.1016/j.chemgeo.2011.09.002

Algeo, T., and Tribovillard, N. (2009). Environmental analysis of paleoceanographic systems based on molybdenum-uranium covariation. *Chem. Geol.* 268, 211–225. doi:10.1016/j.chemgeo.2009.09.001

Baar, H., Bacon, M., Brewer, P., and Bruland, K. (1985). Rare earth elements in the pacific and Atlantic oceans. *Geochimica Cosmochimica Acta* 49, 1943–1959. doi:10.1016/0016-7037(85)90089-4

Bornemann, A., Pross, J., Reichelt, K., Herrle, J., Hemleben, C., and Mutterlose, J. (2005). Reconstruction of short-term palaeoceanographic changes during the formation of the late Albian 'niveau breistroffer' black shales (oceanic anoxic event 1d, SE France). *J. Geol. Soc.* 162, 623–639. doi:10.1144/0016-764903-171

Cai, Q., Chen, X., Zhang, B., Liu, A., Han, J., Zhang, G., et al. (2020). Origin of siliceous minerals in the black shale of the Wufeng and Longmaxi formations in the Yichang area,western hubei province: geological significance for shale gas. *Acta Geol. Sin.* 94, 931–946. doi:10.19762/j.cnki.dizhixuebao.2020133

Cai, Q., Hu, M., Kane, O., Li, M., Zhang, B., Hu, Z., et al. (2022a). Cyclic variations in paleoenvironment and organic matter accumulation of the upper ordovician-lower silurian black shale in the middle Yangtze region, south China: implications for tectonic setting, paleoclimate, and seasea-level change. *Mar. Petroleum Geol.* 136, 105477. doi:10.1016/j.marpetgeo.2021.105477

Cai, Q., Hu, M., Zhang, B., Ngia, N., Liu, A., Liao, R., et al. (2022b). Source of silica and its implications for organic matter enrichment in the upper ordovician-lower silurian black shale in western hubei province, China: insights from geochemical and petrological analysis. *Pet. Sci.* 19, 74–90. doi:10.1016/j.petsci.2021.10.012

Cao, J., Wu, M., Chen, Y., Hu, K., Bian, L., Wang, L., et al. (2012). Trace and rare earth element geochemistry of Jurassic mudstones in the northern Qaidam Basin, northwest China. *Geochemistry* 72, 245–252. doi:10.1016/j.chemer.2011.12.002

Chen, J., Zhang, S., Bao, Z., Sun, S., and Wu, Q. (2006). Antisense c-myc fragments induce normal differentiation cycles in HL-60 cells. *Mar. Orig. Pet. Geol.* 36, 49–57. doi:10.1111/j.1365-2362.2006.01589.x

Chen, X., Fan, J., Chen, Q., Tang, L., and Hou, X. (2014). Toward a stepwise kwangsian orogeny. *Sci. China Earth Sci.* 44, 379–387. doi:10.1007/s11430-013-4815-y

Chen, X., Rong, J., Zhou, Z., Zhang, Y., Zhan, R., Liu, J., et al. (2001). Reconstruction of the spatial patterns of desert/loess boundary belt in North China during the Holocene. *Chin. Sci. Bull.*, 1052–1056.

Cox, R., Lowe, D., and Cullers, R. (1995). The influence of sediment recycling and basement composition on evolution of mudrock chemistry in the southwestern United States. *Geochimica Cosmochimica Acta* 59, 2919–2940. doi:10.1016/0016-7037(95)00185-9

Crusius, J., Calvert, S., Pedersen, T., and Sage, D. (1996). Rhenium and molybdenum enrichments in sediments as indicators of oxic, suboxic and sulfidic conditions of deposition. *Earth Planet. Sci. Lett.* 145, 65–78. doi:10.1016/S0012-821X(96)00204-X

Dahl, T., Hammarlund, E., Rasmussen, C., Bond, D., and Canfield, D. (2021). Sulfidic anoxia in the oceans during the Late Ordovician mass extinctions - insights from molybdenum and uranium isotopic global redox proxies. *Earth-Science Rev.* 220, 103748. doi:10.1016/j.earscirev.2021.103748

Dehairs, F., Lambert, C., Chesselet, R., and Risler, N. (1987). The biological production of marine suspended barite and the barium cycle in the Western Mediterranean Sea. *Biogeochemistry* 4, 119–140. doi:10.1007/BF02180151

Delabroye, A., and Vecoli, M. (2010). The end-ordovician glaciation and the hirnantian stage: A global review and questions about late ordovician event stratigraphy. *Earth-Science Rev.* 98, 269–282. doi:10.1016/j.earscirev.2009.10.010

Demaison, G., and Moore, G. (1980). Anoxic environments and oil source bed genesis. *AAPG Bull.* 64, 1179–1231. doi:10.1016/0146-6380(80)90017-0

Ding, J., Zhang, J., Shi, G., Shen, B., Tang, X., Yangt, Z., et al. (2021). Sedimentary environment and organic matter accumulation for the longtan formation shale in xuancheng area. *Acta Sedimentol. Sin.* 39, 324–340. doi:10.14027/j.issn.1000-0550.2020.056

Ding, M., Li, Y., Fan, T., Lash, G., Wei, X., and Zhang, T. (2023). Geochemistry of the lower silurian black shales from the upper Yangtze platform, south China: implications for paleoclimate, provenance, and tectonic setting. *J. Asian Earth Sci.* 242, 105493. doi:10.1016/j.jseaes.2022.105493

Dong, Z., Wang, Z., Zhang, W., Cheng, S., Fu, X., and Wang, C. (2022). Distribution characteristics and genesis of marine anoxic conditions in the southwest of the upper Yangtze Basin during the late ordovician-early silurian, south China. *Front. Earth Sci.* 10. doi:10.3389/feart.2022.934488

Dymond, J., Suess, E., and Lyle, M. (1992). Barium in deep-sea sediment: A geochemical proxy for paleoproductivity. *Paleoceanography* 7, 163–181. doi:10.1029/92PA00181

Elderfield, H., and Greaves, M. (1982). The rare earth elements in seawater. *Nature* 296, 214–219. doi:10.1038/296214a0

Elrick, M., Reardon, D., Labor, W., Martin, J., Desrochers, A., and Pope, M. (2013). Orbital-scale climate change and glacioeustasy during the early Late Ordovician (pre-Hirnantian) determined from δ18O values in marine apatite. *Geol* 41, 775–778. doi:10.1130/G34363.1

Fedo, C., Wayne Nesbitt, H., and Young, G. (1995). Unraveling the effects of potassium metasomatism in sedimentary rocks and paleosols, with implications for paleoweathering conditions and provenance. *Geology* 23, 921. doi:10.1130/0091-7613(1995)023<0921:UTEOPM>2.3.CO;2

Feng, G., and Chen, S. (1988). Relationship between the reflectance of bitumen and vitrinite in rock. *Natural Gas Industry*, 20-25+7.

Feng, Y., Xiao, X., Gao, P., Wang, E., Hu, D., Liu, R., et al. (2023). Restoration of sedimentary environment and geochemical features of deep marine Longmaxi shale and its significance for shale gas: A case study of the dingshan area in the Sichuan Basin, south China. *Mar. Petroleum Geol.* 151, 106186. doi:10.1016/j.marpetgeo.2023.106186

Gaillardet, J., Dupré, B., and Allègre, C. (1999). Geochemistry of large river suspended sediments: silicate weathering or recycling tracer? *Geochimica Cosmochimica Acta* 63, 4037–4051. doi:10.1016/S0016-7037(99)00307-5

Gallego Torres, D., Martínez Ruiz, F., Paytan, A., Jiménez Espejo, F., and Ortega-Huertas, M. (2007). Pliocene-holocene evolution of depositional conditions in the eastern mediterranean: role of anoxia vs. productivity at time of sapropel deposition. *Palaeogeogr. Palaeoclimatol. Palaeoecol.* 246, 424–439. doi:10.1016/j.palaeo.2006.10.008

Garzanti, E., Padoan, M., Andò, S., Resentini, A., Vezzoli, G., and Lustrino, M. (2013). Weathering and relative durability of detrital minerals in equatorial climate: sand petrology and geochemistry in the east african rift. *J. Geol.* 121, 547–580. doi:10.1086/673259

Ge, X., Mou, C., Xu, Q., Liu, W., Men, X., He, J., et al. (2021). A study on the enrichment of organic materials in black shales of the Wufeng to Longmaxi Formations in eastern Sichuan Basin. *Sediment. Geol. Tethyan Geol.* 41, 418–435. doi:10.19826/j.cnki.1009-3850.2020.12001

Getaneh, W. (2002). Geochemistry provenance and depositional tectonic setting of the Adigrat Sandstone northern Ethiopia. *J. Afr. Earth Sci.* 35, 185–198. doi:10.1016/S0899-5362(02)00126-4

Guan, Q. (2020). *Fine characterization and sweet spot prediction of the wufeng-longmaxi formations in weiyuan area,Sichuan Basin*. doctoral thesis. Beijing, China: China University of Petroleum.

Guo, X. (2017). Sequence stratigraphy and evolution model of the wufeng-longmaxi shale in the upper Yangtze area. *Earth Sci.* 42, 1069–1082. doi:10.3799/dpkx.2017.086

Guo, X., Zhao, Y., Shen, B., Wei, X., Lu, L., et al. (2022). Marine shale gas exploration theory in southern China:review and prospects. *Acta Geol. Sin.* 96, 172–182. doi:10.19762/j.cnki.dizhixuebao.2022271

Haq, B., and Schutter, S. (2008). A chronology of Paleozoic sea-level changes. *Science* 322, 64–68. doi:10.1126/science.1161648

Hatch, J., and Leventhal, J. (1992). Relationship between inferred redox potential of the depositional environment and geochemistry of the Upper Pennsylvanian (Missourian) Stark Shale Member of the Dennis Limestone, Wabaunsee County, Kansas, U.S.A. *Chem. Geol.* 99, 65–82. doi:10.1016/0009-2541(92)90031-Y

He, D., Li, Y., Yang, W., Chen, S., Sun, H., Li, P., et al. (2022). Molecular diagnosis for growth hormone deficiency in Chinese children and adolescents and evaluation of impact of rare genetic variants on treatment efficacy of growth hormone. *Earth Sci. Front.* 524, 1–10. doi:10.1016/j.cca.2021.11.021

Hu, R., Tan, J., Dick, J., Wang, Y., Li, G., and Liu, C. (2023). Depositional conditions of siliceous microfossil-rich shale during the Ordovician-Silurian transition of south China: implication for organic matter enrichment. *Mar. Petroleum Geol.* 154, 106307. doi:10.1016/j.marpetgeo.2023.106307

Huo, Z., Zhang, J., Li, P., Tang, X., Yang, X., Qiu, Q., et al. (2018). An improved evaluation method for the brittleness index of shale and its application-A case study from the southern north China basin. *J. Nat. Gas Sci. Eng.* 59, 47–55. doi:10.1016/j.jngse.2018.08.014

Ibach, L. (1982). Relationship Between Sedimentation Rate and Total Organic Carbon Content in Ancient Marine Sediments. *AAPG Bull.* 66, 170–188. doi:10.1306/03B59A5D-16D1-11D7-8645000102C1865D

Jacob, H. (1989). Classification, structure, genesis and practical importance of natural solid oil bitumen ("migrabitumen"). *Int. J. Coal Geol.* 11, 65–79. doi:10.1016/0166-5162(89)90113-4

Jacob, H. (1985). Disperse solid bitumens as an indicator for migration and maturity in prospecting for oil and gas. *Erdoel Kohle, Erdgas, Petrochem.; Ger. Fed. Repub. Of.* 38, 8.

Jarvie, D., Hill, R., Ruble, T., and Pollastro, R. (2007). Unconventional shale-gas systems: the mississippian Barnett Shale of north-central Texas as one model for thermogenic shale-gas assessment. *Bulletin* 91, 475–499. doi:10.1306/12190606068

Jin, J., Zhan, R., and Wu, R. (2018). Equatorial cold-water tongue in the Late Ordovician. *Geology* 46, 759–762. doi:10.1130/G45302.1

Jin, Q., Zhu, Y. G., and Wang, J. (2008). Deposition and distribution of high-potential source rocks in saline lacustrine environments. *J. China Univ. Petroleum*, 19–23.

Jones, B., and Manning, D. A. (1994). Comparison of geochemical indices used for the interpretation of palaeoredox conditions in ancient mudstones. *Chem. Geol.* 111, 111–129. doi:10.1016/0009-2541(94)90085-X

Khaled, A., Li, R., Xi, S., Zhao, B., Wu, X., Yu, Q., et al. (2022). Paleoenvironmental conditions and organic matter enrichment of the Late Paleoproterozoic Cuizhuang Formation dark shale in the Yuncheng Basin, North China. *J. Petroleum Sci. Eng.* 208, 109627. doi:10.1016/j.petrol.2021.109627

Khan, M., Feng, Q., Zhang, K., and Guo, W. (2019). Biogenic silica and organic carbon fluxes provide evidence of enhanced marine productivity in the Upper Ordovician-Lower Silurian of South China. *Palaeogeogr. Palaeoclimatol. Palaeoecol.* 534, 109278. doi:10.1016/j.palaeo.2019.109278

Kozik, N., Gill, B., Owens, J., Lyons, T., and Young, S. (2022). Geochemical Records Reveal Protracted and Differential Marine Redox Change Associated With Late Ordovician Climate and Mass Extinctions. *AGU Adv.* 3. doi:10.1029/2021AV000563

Li, J., Li, H., Yang, C., Wu, Y., Gao, Z., and Jiang, S. (2022). Geological Characteristics and Controlling Factors of Deep Shale Gas Enrichment of the Wufeng-Longmaxi Formation in the Southern Sichuan Basin China. *Lithosphere* 2022. doi:10.2113/2022/4737801

Li, Q., Lan, B., Li, G., Xu, S., Liu, T., Gou, Q., et al. (2021). Geochemical Characteristics of Element and Their Geological Significance of Wufeng-Longmaxi Formation Shales in North Margin of the Central Guizhou Uplift. *Earth Sci.*, 1–20. doi:10.3799/dqkx.2020.354

Li, S., Xiao, K., Wo, Y., Long, S., and Cai, L. (2008). Developmental Controlling Factors of Upper Ordovician - Lower Silurian High Quality Source Rocks in Marine Sequence, South China. *Acta Sedimentol. Sin.*, 872–880. doi:10.140271/j.cnki.cjxb.2008.05.019

Li, S., Zhou, Z., Nie, H., Liu, M., Meng, F., Shen, B., et al. (2023). Organic matter accumulation mechanisms in the Wufeng-Longmaxi shales in western Hubei Province, China and paleogeographic implications for the uplift of the Hunan-Hubei Submarine high. *Int. J. Coal Geol.* 270, 104223. doi:10.1016/j.coal.2023.104223

Li, Y., Lv, H., Zhang, Y., Zhang, X. L., Shao, D., Yan, J., et al. (2015). U-Mo covariation in marine shales of Wufeng-Longmaxi Formations in Sichuan Basin, China and its implication for identification of watermass restriction. *Geochimica* 44, 109–116. doi:10.19700/j.0379-1726.2015.02.001

Liang, D., Guo, T., Bian, L., Chen, J., and Zhao, Z. (2009). Some Progresses on Studies of Hydrocarbon Generation and Accumulation in Marine Sedimentary Regions,Southern China (Part 3): controlling factors on the Sedimentary Facies and Development of Palaeozoic Marine Source Rocks. *Mar. Orig. Pet. Geol.* 14, 1–19.

Liang, F., Wang, H., Bai, W., Guo, W., Zhao, Q., Sun, S., et al. (2017). Graptolite correlation and sedimentary characteristics of Wufeng-Longmaxi shale in southern Sichuan Basin. *Nat. Gas. Ind.* 37, 20–26. doi:10.3787/j.issn.1000-0976.2017.07.003

Liang, F., Zhang, Q., Xiong, X., Cui, H., Liang, P., and Ma, C. (2019). Sedimentary Evolution Model of Upper Ordovician Wufeng-Lower Silurian Longmaxi Organic-rich Shale in the Sichuan Basin and Its Surrounding Area. *Acta Sedimentol. Sin.* 37, 847–857. doi:10.14027/j.issn.1000-0550.2018.164

Liu, D., and Shi, J. (1994). Discussion on unconventional evaluation method of high evolution carbonate source rock. *Pet. Explor. Dev.*, 113–115.

Liu, S., Ma, W., Luba, J., Huang, W., Zeng, X., Zhang, C., et al. (2011). Characteristics of the shale gas reservoir rocks in the Lower Silurian Longmaxi Formation, East Sichuan basin, China. *Acta Petrol. Sin.* 27, 2239–2252.

Liu, Z., Algeo, T. J., Guo, X., Fan, J., Du, X., and Lu, Y. (2017). Paleo-environmental cyclicity in the Early Silurian Yangtze Sea (South China): tectonic or glacio-eustatic control? *Palaeogeogr. Palaeoclimatol. Palaeoecol.* 466, 59–76. doi:10.1016/j.palaeo.2016.11.007

Lu, Y., Hao, F., Lu, Y., Yan, D., Xu, S., Shu, Z., et al. (2020). Lithofacies and depositional mechanisms of the Ordovician-Silurian Wufeng-Longmaxi organic-rich shales in the Upper Yangtze area, southern China. *Bulletin* 103, 97–129. doi:10.1306/04301918099

Lu, Y., Hao, F., Shen, J., Lu, Y., Song, H., Wang, Y., et al. (2022). High-resolution volcanism-induced oceanic environmental change and its impact on organic matter accumulation in the Late Ordovician Upper Yangtze Sea. *Mar. Petroleum Geol.* 136, 105482. doi:10.1016/j.marpetgeo.2021.105482

Lu, Y., Huang, C., Jiang, S., Zhang, J., Lu, Y., and Liu, Y. (2019). Cyclic late Katian through Hirnantian glacioeustasy and its control of the development of the organic-rich Wufeng and Longmaxi shales, South China. *Palaeogeogr. Palaeoclimatol. Palaeoecol.* 526, 96–109. doi:10.1016/j.palaeo.2019.04.012

Ma, Y., Cai, X., and Zhao, P. (2018). China's shale gas exploration and development: Understanding and practice. *Petroleum Explor. Dev.* 45, 589–603. doi:10.1016/s1876-3804(18)30065-x

McLennan, S., Hemming, S., McDaniel, D., and Hanson, G. (1993). *Geochemical approaches to sedimentation, provenance, and tectonics*. Boulder, Colorado, United States: Special Papers-Geological Society of America.

Melchin, M., Mitchell, C., Holmden, C., and Storch, P. (2013). Environmental changes in the Late Ordovician-early Silurian: review and new insights from black shales and nitrogen isotopes. *GSA Bull.* 125, 1635–1670. doi:10.1130/B30812.1

Munnecke, A., Calner, M., Harper, D., and Servais, T. (2010). Ordovician and Silurian sea-water chemistry, sea level, and climate: A synopsis. *Palaeogeogr. Palaeoclimatol. Palaeoecol.* 296, 389–413. doi:10.1016/j.palaeo.2010.08.001

Murphy, A., Sageman, B., Hollander, D., Lyons, T., and Brett, C. (2000). Black shale deposition and faunal overturn in the Devonian Appalachian Basin: clastic starvation, seasonal water-column mixing, and efficient biolimiting nutrient recycling. *Paleoceanography* 15, 280–291. doi:10.1029/1999PA000445

Murray, R., Buchholtz Ten Brink, M., Gerlach, D., Russ, G., and Jones, D. (1991). Rare earth, major, and trace elements in chert from the Franciscan Complex and Monterey Group, California: assessing REE sources to fine-grained marine sediments. *Geochimica Cosmochimica Acta* 55, 1875–1895. doi:10.1016/0016-7037(91)90030-9

Murray, R. (1994). Chemical criteria to identify the depositional environment of chert: general principles and applications. *Sediment. Geol.* 90, 213–232. doi:10.1016/0037-0738(94)90039-6

Murray, R., and Leinen, M. (1993). Chemical transport to the seafloor of the equatorial Pacific Ocean across a latitudinal transect at 135°W: tracking sedimentary major, trace, and rare earth element fluxes at the Equator and the Intertropical Convergence Zone. *Geochimica Cosmochimica Acta* 57, 4141–4163. doi:10.1016/0016-7037(93)90312-K

Nakagawa, Y., Takano, S., Firdaus, M., Norisuye, K., Hirata, T., Vance, D., et al. (2012). The molybdenum isotopic composition of the modern ocean. *Geochem. J.* 46, 131–141. doi:10.2343/geochemj.1.0158

Nesbitt, H., and Young, G. (1982). Early Proterozoic climates and plate motions inferred from major element chemistry of lutites. *Nature* 299, 715–717. doi:10.1038/299715a0

Nesbitt, H., Young, G., McLennan, S., and Keays, R. (1996). Effects of Chemical Weathering and Sorting on the Petrogenesis of Siliciclastic Sediments, with Implications for Provenance Studies. *J. Geol.* 104, 525–542. doi:10.1086/629850

Nesbitt, H., and Young, G. (1984). Prediction of some weathering trends of plutonic and volcanic rocks based on thermodynamic and kinetic considerations. *Geochimica Cosmochimica Acta* 48, 1523–1534. doi:10.1016/0016-7037(84)90408-3

Nie, H., Jin, Z., Ma, X., Liu, Z., Lin, T., and Yang, Z. (2017). Dispositional characteristics of Ordovician Wufeng Formation and Silurian Longmaxi Formation in Sichuan Basin and its adjacent areas. *Petroleum Res.* 2, 233–246. doi:10.1016/j.ptlrs.2017.01.003

Paytan, A., Kastner, M., and Chavez, F. (1996). Glacial to Interglacial Fluctuations in Productivity in the Equatorial Pacific as Indicated by Marine Barite. *Science* 274, 1355–1357. doi:10.1126/science.274.5291.1355

Pedersen, T., and Calvert, S. (1990). Anoxia vs. Productivity: what Controls the Formation of Organic-Carbon-Rich Sediments and Sedimentary Rocks? (1). *AAPG Bull.* 74. doi:10.1306/0C9B232B-1710-11D7-8645000102C1865D

Peng, J. (2021). Sedimentology of the Upper Pennsylvanian organic-rich Cline Shale, Midland Basin: from gravity flows to pelagic suspension fallout. *Sedimentology* 68, 805–833. doi:10.1111/sed.12811

Perri, F. (2018). Reconstructing chemical weathering during the Lower Mesozoic in the Western-Central Mediterranean area: a review of geochemical proxies. *Geol. Mag.* 155, 944–954. doi:10.1017/S0016756816001205

Pi, D., Liu, C., Zhou, S., and Jiang, S. (2013). Trace and rare earth element geochemistry of black shale and kerogen in the early Cambrian Niutitang Formation in Guizhou province, South China: constraints for redox environments and origin of metal enrichments. *Precambrian Res.* 225, 218–229. doi:10.1016/j.precamres.2011.07.004

Pohl, A., Donnadieu, Y., Le Hir, G., and Ferreira, D. (2017). The climatic significance of Late Ordovician-early Silurian black shales. *Paleoceanography* 32, 397–423. doi:10.1002/2016PA003064

Qiu, Z., Liu, B., Dong, D., Lu, B., Yawar, Z., Chen, Z., et al. (2020a). Silica diagenesis in the Lower Paleozoic Wufeng and Longmaxi Formations in the Sichuan Basin, South China: implications for reservoir properties and paleoproductivity. *Mar. Petroleum Geol.* 121, 104594. doi:10.1016/j.marpetgeo.2020.104594

Qiu, Z., Wei, H., Liu, H., Shao, N., Wang, Y., Zhang, L., et al. (2021). Accumulation of sediments with extraordinary high organic matter content: insight gained through geochemical characterization of indicative elements. *Oil Gas Geol.* 42, 931–948. doi:10.11743/ogg20210414

Qiu, Z., and Zou, C. (2020a). Controlling factors on the formation and distribution of "sweet-spot areas" of marine gas shales in South China and a preliminary discussion on unconventional petroleum sedimentology. *J. Asian Earth Sci.* 194, 103989. doi:10.1016/j.jseaes.2019.103989

Qiu, Z., and Zou, C. (2020b). Unconventional Petroleum Sedimentology:Connotation and prospect. *Acta Sedimentol. Sin.* 38, 1–29. doi:10.14027/j.issn.1000-0550.2019.116

Qiu, Z., Zou, C., Wang, H., Dong, D., Lu, B., Chen, Z., et al. (2020b). Discussion on characteristics and controlling factors of differential enrichment of Wufeng-Longmaxi formations shale gas in South China. *Nat. Gas. Geosci.* 31, 163–175. doi:10.11764/j.issn.1672-1926.2019.11.003

Rimmer, S., Thompson, J., Goodnight, S., and Robl, T. (2004). Multiple controls on the preservation of organic matter in Devonian-Mississippian marine black shales: geochemical and petrographic evidence. *Palaeogeogr. Palaeoclimatol. Palaeoecol.* 215, 125–154. doi:10.1016/s0031-0182(04)00466-3

Rong, J. (1984). Ecological and stratigraphic evidence of the Late Ordovician regression and its association with glacial activity in the Upper Yangtze region. *J. Of Stratigr.*, 19–29. doi:10.19839/j.cnki.dcxzz.1984.01.003

Rong, J., and Huang, B. (2019). An indicator of the onset of the end Ordovician mass extinction in South China: the Manosia brachiopod assemblage and its diachronous distribution. *Acta Geol. Sin.* 93, 509–527. doi:10.19762/j.cnki.dizhixuebao.2019066

Ross, D., and Bustin, R. (2009). Investigating the use of sedimentary geochemical proxies for paleoenvironment interpretation of thermally mature organic-rich strata: examples from the Devonian-Mississippian shales, Western Canadian Sedimentary Basin. *Chem. Geol.* 260, 1–19. doi:10.1016/j.chemgeo.2008.10.027

Sageman, B., Murphy, A., Werne, J., Ver Straeten, C., Hollander, D., and Lyons, T. (2003). A tale of shales: the relative roles of production, decomposition, and dilution in the accumulation of organic-rich strata, Middle-Upper Devonian, Appalachian basin. *Chem. Geol.* 195, 229–273. doi:10.1016/S0009-2541(02)00397-2

Schoepfer, S., Shen, J., Wei, H., Tyson, R., Ingall, E., and Algeo, T. (2015). Total organic carbon, organic phosphorus, and biogenic barium fluxes as proxies for paleomarine productivity. *Earth-Science Rev.* 149, 23–52. doi:10.1016/j.earscirev.2014.08.017

Schulte, S., Mangelsdorf, K., and Rullkötter, J. (2000). Organic matter preservation on the Pakistan continental margin as revealed by biomarker geochemistry. *Org. Geochem.* 31, 1005–1022. doi:10.1016/S0146-6380(00)00108-X

Scott, C., and Lyons, T. (2012). Contrasting molybdenum cycling and isotopic properties in euxinic versus non-euxinic sediments and sedimentary rocks: refining the paleoproxies. *Chem. Geol.* 324-325, 19–27. doi:10.1016/j.chemgeo.2012.05.012

Shields, G., and Stille, P. (2001). Diagenetic constraints on the use of cerium anomalies as palaeoseawater redox proxies: an isotopic and REE study of Cambrian phosphorites. *Chem. Geol.* 175, 29–48. doi:10.1016/S0009-2541(00)00362-4

Shu, L. (2021). Principal features of intracontinental orogenic belt and discussions on its dynamics. *Acta Geol. Sin.* 95, 98–106. doi:10.19762/j.cnki.dizhixuebao.2020287

Shu, L., Wang, B., Cawood, P. A., Santosh, M., and Xu, Z. (2015). Early Paleozoic and Early Mesozoic intraplate tectonic and magmatic events in the Cathaysia Block, South China. *Tectonics* 34, 1600–1621. doi:10.1002/2015TC003835

Su, W., Huff, W., Ettensohn, F., Liu, X., Zhang, J., and Li, Z. (2009). K-bentonite, black-shale and flysch successions at the Ordovician-Silurian transition, South China: possible sedimentary responses to the accretion of Cathaysia to the Yangtze Block and its implications for the evolution of Gondwana. *Gondwana Res.* 15, 111–130. doi:10.1016/j.gr.2008.06.004

Su, W., Li, Z., Frang, R., Markes, E., Warren, D., Wang, W., et al. (2007). Distribution of Black Shale in the Wufeng-Longmaxi Formations (Ordovician-Silurian).South China: major Controlling Factors and Implications. *Earth Science-Journal China Univ. Geosciences* 32, 819–827.

Sweere, T., van den Boorn, S., Dickson, A., and Reichart, G. (2016). Definition of new trace-metal proxies for the controls on organic matter enrichment in marine sediments based on Mn, Co, Mo and Cd concentrations. *Chem. Geol.* 441, 235–245. doi:10.1016/j.chemgeo.2016.08.028

Taylor, S., and McLennan, S. (1985). *The continental crust: Its composition and evolution*. Palo Alto, CA, USA: Blackwell Scientific.

Torsvik, T., and Cocks, L. (2013). Gondwana from top to base in space and time. *Gondwana Res.* 24, 999–1030. doi:10.1016/j.gr.2013.06.012

Tribovillard, N., Algeo, T., Baudin, F., and Riboulleau, A. (2012). Analysis of marine environmental conditions based onmolybdenum-uranium covariation-Applications to Mesozoic paleoceanography. *Chem. Geol.* 324-325, 46–58. doi:10.1016/j.chemgeo.2011.09.009

Tribovillard, N., Algeo, T., Lyons, T., and Riboulleau, A. (2006). Trace metals as paleoredox and paleoproductivity proxies: an update. *Chem. Geol.* 232, 12–32. doi:10.1016/j.chemgeo.2006.02.012

Tyson, R., and Pearson, T. (1991). Modern and ancient continental shelf anoxia: an overview. *SP* 58, 1–24. doi:10.1144/GSL.SP.1991.058.01.01

Van De Kamp, P., and Leake, B. (1985). Petrography and geochemistry of feldspathic and mafic sediments of the northeastern Pacific margin. *Trans. R. Soc. Edinb. Earth Sci.* 76, 411–449. doi:10.1017/S0263593300010646

Van Den Boorn, S., Van Bergen, M., Nijman, W., and Vroon, P. (2007). Dual role of seawater and hydrothermal fluids in Early Archean chert formation: evidence from silicon isotopes. *Geol* 35, 939. doi:10.1130/G24096A.1

Wang, C., Chen, X., and Wang, X. (2002). Changes Of Detrital Composition Of The Paleogene Sandstones In South Jinxian Sag Of Jizhong Basin And Its Sequence Significance. *J. Of Stratigr.*, 272–279+285.

Wang, J., Huang, X., Sui, J., Shao, H., Yan, C., Wang, S., et al. (1997). Evolutional Characteristics and Their Paleoclimate Significance of Trace Elements in the Hetaoyuan Formation,Biyang Depression. *Acta Sedimentol. Sin.* 15, 65–68. doi:10.14027/j.cnki.cjxb.1997.01.012

Wang, T., Zhang, K., Xiong, L., Shi, H., Song, X., Wei, L., et al. (2018). Paleogeomorphology restoration of Wufeng Formation-Lower Member of Longmaxi Formation in Zigong areaof Sichuan Province and its oil and gas significance. *Petroleum Geol. Exp.* 40, 764–770. doi:10.11781/sysydz201806764

Wang, Y., Dong, D., Huang, J., Li, X., and Wang, S. (2016). Guanyinqiao Member lithofacies of the Upper Ordovician Wufeng Formation around the Sichuan Basin and the significance to shale gas plays,SW China. *Petroleum Explor. Dev.* 43, 45–53. doi:10.1016/s1876-3804(16)30005-2

Wang, Y. M., Li, X. J., Dong, D. Z., Zhang, C. C., and Wang, S. F. (2017). Main factors controlling the sedimentation of high-quality shale in Wufeng-Longmaxi Fm,Upper Yangtze region. *Nat. Gas. Ind.* 37, 9–20. doi:10.3787/j.issn.1000-0976.2017.04.002

Wedepohl, K. (1971). Environmental influences on the chemical composition of shales and clays. *Phys. Chem. Earth* 8, 307–333. doi:10.1016/0079-1946(71)90020-6

Wei, H., Hu, J., Wang, L., Xu, F., and Wang, S. (2012). Productivity and redox proxies of palaeo-oceans:An overview of elementary geochemistry. *Sediment. Geol. Tethyan Geol.* 32, 76–78. doi:10.1016/j.ab.2012.06.027

Wignall, P., and Twitchett, R. (1996). Oceanic Anoxia and the End Permian Mass Extinction. *Science* 272, 1155–1158. doi:10.1126/science.272.5265.1155

Wilde, P., Quinby-Hunt, M., and Erdtmann, B. (1996). The whole-rock cerium anomaly: a potential indicator of eustatic sea-level changes in shales of the anoxic facies. *Sediment. Geol.* 101, 43–53. doi:10.1016/0037-0738(95)00020-8

Wu, Y., Zhang, P., He, X., Gao, Y., He, G., Sun, B., et al. (2020). Lithofacies and shale gas enrichment of Wufeng Formation-Longmaxi Formation in Southeastern Chongqing. *Mar. Orig. Pet. Geol.* 25, 335–343. doi:10.3969/j.issn.1672-9854.2020.04.006

Xu, L., Huang, S., Wang, Y., Zhou, X., Liu, Z., Wen, Y., et al. (2023). Palaeoenvironment evolution and organic matter enrichment mechanisms of the Wufeng-Longmaxi shales of Yuanán block in western Hubei, middle Yangtze: implications for shale gas accumulation potential. *Mar. Petroleum Geol.* 152, 106242. doi:10.1016/j.marpetgeo.2023.106242

Xu, Y., Cawood, P., and Du, Y. (2016). Intraplate orogenesis in response to Gondwana assembly: kwangsian Orogeny, South China. *Am. J. Sci.* 316, 329–362. doi:10.2475/04.2016.02

Yan, D., Chen, D., Wang, Q., and Wang, J. (2009). Geochemical changes across the Ordovician-Silurian transition on the Yangtze Platform, South China. *Sci. China Ser. D Earth Sci.* 52, 38–54. doi:10.1007/s11430-008-0143-z

Yan, D., Li, S., Fu, H., Jasper, D. M., Zhou, S., Yang, X., et al. (2021). Mineralogy and geochemistry of Lower Silurian black shales from the Yangtze platform, South China. *Int. J. Coal Geol.* 237, 103706. doi:10.1016/j.coal.2021.103706

Yan, D., Wang, H., Fu, Q., Chen, Z., He, J., and Gao, Z. (2015). Geochemical characteristics in the Longmaxi Formation (Early Silurian) of South China: implications for organic matter accumulation. *Mar. Petroleum Geol.* 65, 290–301. doi:10.1016/j.marpetgeo.2015.04.016

Yang, S., Hu, W., Fan, J., and Deng, Y. (2022). New geochemical identification fingerprints of volcanism during the Ordovician-Silurian transition and its implications for biological and environmental evolution. *Earth-Science Rev.* 228, 104016. doi:10.1016/j.earscirev.2022.104016

Zhang, B., Chen, X., Cai, Q., Chen, L., Zhang, H., and Li, P. (2022). Dominant shale lithofacies and gas generation potential analysis of the Wufeng-Longmaxi Formation in the Yichang slope area,Western Hubei Province. *Geol. China* 49, 943–955. doi:10.2029/gc20220318

Zhang, C., Liu, Z., Dong, D., Jiang, S., Guan, Q., Ji, M., et al. (2019). Tau-TCHF Inhibits Spleenic Apoptosis via PI3K-Akt Signaling Pathway in Chickens. *Xinjiang Pet. Geol.* 40, 555–563. doi:10.1007/978-981-13-8023-5_51

Zhang, J., Mou, C., Zhou, K., Feng, L., Wu, H., Chen, X., et al. (2017a). The Combined Antitumor Effects of ^{125}I Radioactive Particle Implantation and Cytokine-Induced Killer Cell Therapy on Xenograft Hepatocellular Carcinoma in a Mouse Model. *Acta Geol. Sin.* 91, 1083–1091. doi:10.1177/1533034617732204

Zhang, R., Jin, Z., Zhu, R., Li, M., Hui, P., Wei, R., et al. (2023). Investigation of deposition rate of terrestrial organic-rich shales in China and its implications for shale oil exploration. *Oil Gas Geol.* 44, 829–845. doi:10.11743/ogg20230403

Zhang, S., Wang, X., Wang, H., Bjerrum, C. J., Hammarlund, E. U., Costa, M. M., et al. (2016). Sufficient oxygen for animal respiration 1,400 million years ago. *Proc. Natl. Acad. Sci. U. S. A.* 113, 1731–1736. doi:10.1073/pnas.1523449113

Zhang, S., Zhang, B., Bian, Z., Chen, Jin, Z., Wang, D., et al. (2005). Development constraints of marine source rocks in China. *Earth Sci. Front.*, 39–48.

Zhang, X. S., Xu, X. S., Xia, Y., and Liu, L. (2017b). Early Paleozoic intracontinental orogeny and post-orogenic extension in the South China Block: insights from volcanic rocks. *J. Asian Earth Sci.* 141, 24–42. doi:10.1016/j.jseaes.2016.07.016

Zhang, Y., Fan, C., Zhong, C., Ye, Z., Qin, Q., et al. (2018). Study on the Evaluation Method of Organic -Rich Shale Brittleness in Complex Geological Conditions. *Geol. Explor.* 54, 1069–1083. doi:10.13712/j.cnki.dzykt.2018.05.018

Zhang, Y., Zhan, R., Zhen, Y., Fang, X., and Zhang, J. (2020). Challenges and Future Perspectives of Ordovician Studies in China. *J. Stratigr.* 44, 339–348. doi:10.19839/j.cnki.dcxzz.2020.0042

Zhao, L., Li, Y., Zou, C., Zhao, S., and Wu, C. (2023). Palaeoweathering Conditions, Provenance, and Tectonic Setting of the Early Silurian Longmaxi Formation in the Upper Yangtze Region (Southern China): evidence from Geochemistry. *Minerals* 13, 576. doi:10.3390/min13040576

Zhao, Z., Zhao, J., Wang, H., Liao, J., and Liu, C. (2007). Distribution Characteristics And Applications Of Trace Elements In Junggar Basin. *Nat. Gas Explor. Dev.*, 30–32+40+77.

Zheng, Y., Anderson, R. F., van Geen, A., and Fleisher, M. Q. (2002). Preservation of particulate non-lithogenic uranium in marine sediments. *Geochimica Cosmochimica Acta* 66, 3085–3092. doi:10.1016/S0016-7037(01)00632-9

Zhu, Y., Chen, G., Liu, Y., Shi, X., Wu, W., Luo, C., et al. (2021). Sequence stratigraphy and lithofacies paleogeographic evolution of Katian Stage-Aeronian Stage in southern Sichuan Basin,SW China. *Petroleum Explor. Dev.* 48, 1126–1138. doi:10.1016/s1876-3804(21)60096-4

Zou, C., Qiu, Z., Poulton, S. W., Dong, D., Wang, H., Chen, D., et al. (2018). Ocean euxinia and climate change "double whammy" drove the Late Ordovician mass extinction. *Geology* 46, 535–538. doi:10.1130/G40121.1

Zou, C., Zhu, R., Chen, Z., Ogg, J. G., Wu, S., Dong, D., et al. (2019). Organic-matter-rich shales of China. *Earth-Science Rev.* 189, 51–78. doi:10.1016/j.earscirev.2018.12.002